Deep Sea Research Part I: Oceanographic Research Papers
April 2023, Volume 194, Pages 103951 (11p.)
https://doi.org/10.1016/j.dsr.2022.103951
https://archimer.ifremer.fr/doc/00813/92535/

Distribution of Pa in the Atlantic sector of the Southern Ocean: Tracking scavenging during water mass mixing along neutral density surfaces

Levier M. [1, *], Roy-Barman M. [3], Foliot L. [1], Dapoigny A. [1], Lacan F. [2]

[1] Laboratoire des Sciences du Climat et de l'Environnement (LSCE), Gif-sur-Yvette, France
[2] Laboratoire d'Etude de Géophysique et Océanographie Spatiale (LEGOS), Toulouse, France
[3] Laboratory for Sciences of Climate and Environment, France

* Corresponding author : M. Levier, email address : martin.levier@lsce.ipsl.fr

Abstract :

Dissolved and particulate Protactinium-231 (231Pa) was analyzed for samples from the BONUS GoodHope (BGH) IPY-GEOTRACES cruise in the SE Atlantic sector of the Southern Ocean (36°S-13°E to 57°S-0°, Feb.–Mar. 2008). The inflowing waters from the Atlantic Ocean fuel the Antarctic Circumpolar Current in dissolved 231Pa which is mostly removed from seawater by the biogenic silica produced by diatoms in the Southern Ocean. This scavenging flux of the 231Pa induces a meridional gradient of the 231Pa concentration and of the Th–Pa fractionation factor (FTh/Pa).

We propose a first direct estimate of the 231Pa partition coefficient between suspended opal and seawater of about $1.42 \pm 0.55 \times 106$ g/g. This partition coefficient could directly apply to simulate the particulate Pa concentration from the dissolved fraction and the opal concentration. We apply to 231Pa the isopycnal advection-diffusion-scavenging model built for Th isotopes across the ACC. This additional constraint on the model does not modify the isopycnal eddy diffusion estimate of about 1900 ± 180 m2/s at different isopycnal surfaces but suggests a higher particle settling velocity, about 1000 m/y, in the northern part of the ACC than solely derived from Th isotopes. The most different feature is the reduction by half of the estimated uncertainties among the different transport parameters just by the addition of a new constraining parameter. Moreover, this study confirms that 231Pa budget of the Atlantic Sector of Southern Ocean cannot be balanced by considering meridional transport only, and need to consider eastward export to scavenge Pa in the whole area of the Opal Belt.

Highlights

► Measurements of ^{231}Pa in new seawater samples from the Atlantic sector of Southern Ocean. ► New determination of the partition coefficient of the ^{231}Pa on the opal particle phase. ► Assessment of the advection-diffusion-scavenging model along isopycnal by an application to the ^{231}Pa data across the Southern Ocean.

Keywords : Protactinium, Mass spectrometry, marine particles, Southern Ocean, isopycnal mixing

1. Introduction

Protactinium-231 (^{231}Pa) is a radioactive isotope produced at a constant rate in seawater by the uranium-235 (^{235}U) decay. Dissolved ^{231}Pa has a residence time in seawater of about 100 years controlled by scavenging by marine particles, so most of the ^{231}Pa produced *in situ* is transported toward the sediment (Anderson et al., 1983; Edmonds et al., 1998). Thorium-230 (^{230}Th) is also a particle reactive isotope produced at a constant rate in seawater by the decay of uranium-234 (^{234}U). The difference of particle reactivity of ^{231}Pa and ^{230}Th induces deviations of the ^{231}Pa/^{230}Th ratios of seawater, marine particles and sediments from the production activity ratio (0.093) (Rutgers van der Loeff and Berger, 1993). The Pa/Th ratio in sediments is used as a paleoproxy of the ventilation of deep water in the meridional circulation of the Atlantic Ocean assuming an accumulation of ^{231}Pa in dissolved fraction (Lippold et al., 2012; McManus et al., 2004; Yu et al., 1996). However, recent studies on Pa/Th content on Atlantic seawater shows almost no variation of dissolved ratio in Atlantic below the equatorial line, and the sediment Pa/Th measured mostly depend on the particle composition of seawater (Deng et al., 2014: Deng et al. 2018; Hayes et al., 2015). South of the Atlantic Ocean, the change of the ^{231}Pa/^{230}Th ratio is attributed to the enhanced scavenging of ^{231}Pa by diatoms (Scholten et al., 2008). While the affinity of ^{231}Pa for biogenic opal is well recognized (Chase et al., 2002; DeMaster, 1981; Gdaniec et al., 2020; Geibert and Usbeck, 2004; Lin et al., 2014; Yu et al., 1996), quantification of the ^{231}Pa affinity for biogenic opal in suspended particles remained poorly constrained (Hayes et al., 2015), while the focusing effect could bias sediment trap record, and laboratory experiment don't consider environment constraints. There is almost no data about the biogenic opal dissolution impact on the ^{231}Pa particulate flux in deep waters (Gdaniec et al., 2020).

^{231}Pa budget of the Atlantic sector of the Southern Ocean shows that the main source of ^{231}Pa to the Antarctic Circumpolar Current (ACC) is the inflow from the Atlantic Ocean, half of it being removed by scavenging in the Weddell gyre (Rutgers van der Loeff et al., 2016). The other half of the inflowing Pa is exported to the Indian and Pacific sectors of the Southern Ocean where ^{231}Pa is also scavenged or exported to the Pacific Ocean through isopycnal mixing (Pavia et al., 2020). The removal of ^{231}Pa upwelling from the South Atlantic in the Weddell gyre results from a double trap : first by the gyre circulation preventing intermediate ^{231}Pa-rich waters to flow northward, enhancing the ^{231}Pa scavenging in the center of the gyre, and second by Pa scavenging in the opal belt (area of high diatom production, around 52°S), when Weddell Sea Deep Water (WSDW) flows out the gyre (Rutgers van der Loeff et al., 2016).

Here, we report dissolved and particulate ^{231}Pa data from samples collected across the Antarctic Circumpolar Current (ACC) during the Bonus GoodHope cruise in the Southern sector the Atlantic Ocean. The Bonus GoodHope section samples were previously analyzed for thorium isotopes (Roy-Barman et al., 2019).

Thorium isotope transport across the ACC was described with an advection-diffusion-scavenging model along isopycnal surfaces, allowing estimating isopycnal advection and isopycnal eddy diffusion coefficients as well as particle settling velocity. We present an extension of this model to protactinium isotopes to get further insight in the behavior of ^{231}Pa, notably to determine mixing rate of Pa across the ACC. Finally, ^{230}Th and ^{231}Pa data comparison provides insight in the fractionation of these elements by marine particles.

2. Methods

2.1. Hydrologic context

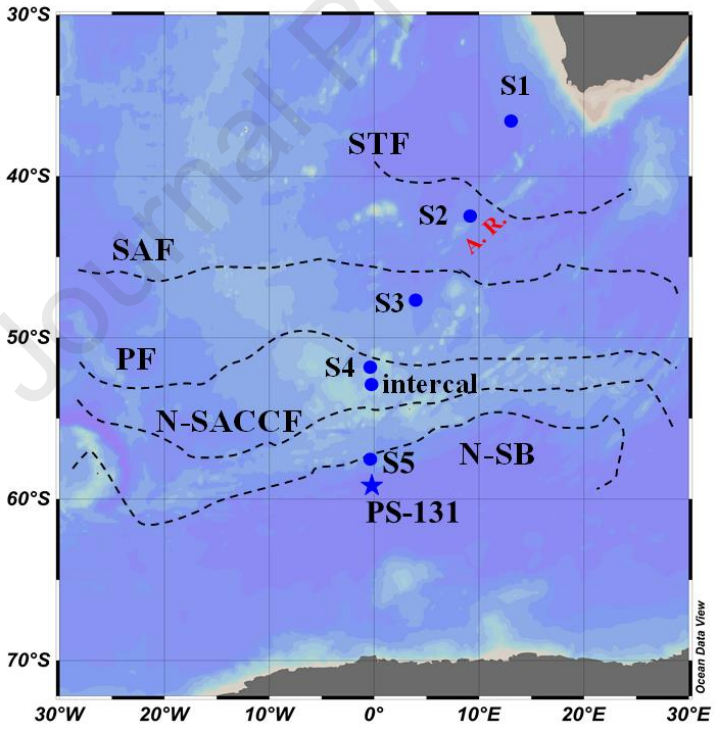

Figure 1 : Map of the stations from the Bonus GoodHope cruise, with the different fronts across the Southern Ocean determined from the mean circulation path (Roy-Barman et al., 2019; Sokolov and Rintoul, 2009)

The main water masses and currents encountered during the Bonus GoodHope cruise were described in detail elsewhere (Abadie et al., 2017; Bown et al., 2011; Chever et al., 2010;

Garcia-Solsona et al., 2014; Roy-Barman et al., 2019). The section is characterized by three main hydrological and circulation domains (Fig. 1): the Subtropical domain (Station S1). The Antarctic Circumpolar Current (ACC; S2 to S4) and the Weddell Sea Gyre (S5). The subtropical domain is bounded to the south by the subtropical front (STF), which was located around 41°S-42°S, north of S2. The ACC domain includes the Subantarctic Front (SAF; ~45°S) and the Polar Front (PF; ~50°S). It is bounded to the south by the southern ACC boundary (Sby). From the Sby to the Antarctica, the cyclonic Weddell Gyre (WG; S5) dominates water circulation.

Water mass transport along the BGH section is mainly zonal. In the subtropical domain (station S1), it is dominated by the westward flowing Agulhas Current in the upper water column ($z < 1500$ m) and at depth by the eastward transport of SE-NADW (Sokolov and Rintoul, 2009). Stations S2, S3 and S4 are located within the Antarctic Circumpolar Current, flowing eastward throughout the water column. Finally, the Weddell gyre is a mainly wind-driven cyclonic gyre (Ryan et al., 2016), constrained by topographic boundaries except in the East, where mixing occurs between ACC and Weddell Gyre water masses (Gouretski and Danilov, 1993; Schröder and Fahrbach, 1999). The Circumpolar Deep Water (CDW) inflowing the Weddell Gyre, is called Warm Deep Water (WDW). It circulates from the East to the West in the southern part of the Weddell Gyre. The WDW is modified by upwelling into and mixing with shallower water and makes its way to the southern part of the Weddell Sea. By cooling and brine rejection during winter, the cold Weddell Sea Deep Water (WSDW) and Weddell Sea Bottom Water (WSBW) are formed (Nicholls et al., 2009) and flow northward, following the cyclonic gyre circulation. A significant fraction of the WSDW is exported to the North and mixes with the ACC at the Scotia Ridge. The remaining fraction flows toward the northeast of the Weddell Gyre, where the station S5 is located. This water partly recirculates in the gyre by mixing with the Circumpolar Deep Water incoming from east to form the new WDW (Deacon, 1979; Gouretski and Danilov, 1993).

The BGH section is approximately perpendicular to the mean flow of the ACC, so the BGH stations are not hydrologically connected and there might be no direct mixing between the stations. However, slower meridional transport rates were noted on meridional sections of water mass tracers such as salinity, temperature or iron isotopes, revealing notably the northward transport of AAIW and AABW, and southward transport of NADW (Abadie et al., 2017; Roy-Barman et al., 2019). This meridional transport is assumed to be a residual flow from the

Atlantic Ocean circulation in which lateral eddy fluxes largely balance the wind-driven circulation (Marshall and Speer, 2012). In the following, we apply a simple transport model of advection-diffusion-scavenging to link tracer properties measured along the BGH meridional section (Roy-Barman et al., 2019). The transports are not assumed to be a true meridional mixing along the BGH section, but it allows to estimate the residual meridional component of the mixing (advection, diffusion) embedded in the dominant zonal of the ACC Atlantic sector.

2.2. Sampling

The BONUS GoodHope cruise occurred from February 8th 2008 to March 17th 2008, during the late austral summer, on board Marion-Dufresne II Research Vessel. Samples were collected along a transect between 34°S 19°E and 51°S 0°W and then along the Greenwich meridian from 51°S to 58°S. Five full depth profiles were sampled (S1-S5 stations) for both dissolved and particulate ^{231}Pa analysis. Three depths were collected for dissolved ^{231}Pa analysis at an intercalibration station, near the station S4. Seawater samples were collected with Niskin bottles mounted on a rosette, equipped with a CTD sensor. Challenger Oceanic in situ pumps (ISP) were used to filter large seawater volumes through SUPOR filters (pore size: 0.45 µm, filter diameter: 293 mm) seawater volumes filtered ranging from 200 L to 1000 L.

2.3. Analytical procedure

2.3.1. Filtered seawater

Ten liters of filtered seawater (Nuclepore^{TM}, 90mm diameter, 0.4 µm pore size) were acidified at pH = 2 with HCl on board. The samples were processed in a clean lab for the simultaneous extraction of ^{227}Ac and ^{231}Pa as describe in Levier et al. (2021). To summarize, samples were spiked with Protactinium-233 (^{233}Pa), previously milked from Neptunium-237 on hydrated silica (Guihou et al., 2010). Pa isotopes were preconcentrated using manganese oxides co-precipitation (Ghaleb et al., 2004; Rutgers van der Loeff and Moore, 1999). The precipitate was recovered on NucleoporeTM filter (diameter 142 mm, 0.45 µm pore size). The precipitate on the filter was dissolved in a bath of 6 M HCl with 100 µL of H_2O_2 and 100 µL of 27 M HF for thirty minutes. The filter was then rinsed with 6 M HCl. After evaporation of the dissolution bath, the residue was dissolved in 0.5 mL of 9 M HCl and loaded on an anion-exchange column (AG1-X8 resin, 200-400 mesh) to separate the protactinium fraction, eluted with 9 M HCl +

143 0.26 M HF, from the major elements, uranium, thorium and rare earth elements (REEs) and
144 actinium (Levier et al., 2021).

145

146 ### 2.3.2. Particulate samples

147 Particulate protactinium was recovered and purified from the particulate thorium isotopes
148 sample batch analysis (Roy-Barman et al., 2019). Filters from the *in situ* pumps were cut into
149 pieces using ceramic scissors. Several leaching steps were necessary to recover Th without
150 attacking the filters. Filter pieces were first leached with 200 mL of 6 M HCl and 1.5 mL of 24-
151 25 M HF in a 300 mL Teflon beaker for 2 days at 75°C. The filter pieces were removed from
152 the leaching solution and rinsed with a MQ water squeeze bottle over the leaching beaker. The
153 filter pieces were saved apart. The leaching and rinsing solutions were evaporated down to
154 ~10 mL and transferred into a 30 mL Teflon beaker. Then, the filter pieces were leached for a
155 second time with 150 mL of 7 M HNO_3 and 0.05 mL of 25 M HF for 2 days at 75°C. The filter
156 pieces were removed from the leaching solution and rinsed with MQ water that was again
157 recovered into the leaching beaker. After evaporation to a few mL, this solution was added to
158 the first leaching and rinsing solution. The 300 mL Teflon beaker was rinsed in warm diluted
159 HNO_3 to remove any particle sticking on the beaker walls and the resulting solution was also
160 added to the 30 mL beaker. The resulting solution was then spiked with ^{233}Pa (and ^{229}Th), dried
161 and dissolved again with 4 mL of 14 M HNO_3 and 1 mL of 12 M HCl. After 1 night on a hot
162 plate at 100°C, the solution was dried and the residue was dissolved again in 10 ml of 1 M
163 HNO_3. Since the filters were not rinsed immediately after filtration with distilled water on board,
164 it was preferable to remove the salt before the column chemistry. Therefore, 40 µL of a Fe
165 solution (60 mg/g) were added. After 1h-heating, Fe was precipitated by raising the pH to about
166 8 with NH_3. The Fe precipitate (that co-precipitates Th and Pa isotopes) was separated by
167 centrifugation and rinsed several times. Finally, it was dissolved in 0.25 ml of 8 M HNO_3, ready
168 for loading on an anionic column. Pa and Th isotopes were separated from Fe by ion exchange
169 chromatography on a small volume (0.5 ml) column of AG1X8 (200-400 mesh) resin (Gdaniec
170 et al., 2018, adapted from Jeandel et al., 2011).

171

172 ## 2.4. Mass spectrometry

173 Every analysis was performed on a Multiple Collection Inductively Coupled Plasma Mass

Spectrometer (MC-ICPMS) Neptune^{plus} (Thermo-Fischer) mounted with a jet interface and an Aridus II desolvatation system based on a protocol derived from Guihou et al., 2010. The acquisition conditions of Pa measurements are given in Gdaniec et al., 2018. The calibration of ^{233}Pa spike solution was made against an in-house ^{231}Pa standard, used for intercalibration exercises (Gdaniec et al., 2019 ; Gdaniec et al., in prep). Particle samples from stations S1 and S2, spike calibration was lost during the chemical separation. This loss made impossible the precise correction for the chemical yield. To circumvent this problem, we noted that for stations S3, S4 and S5, the chemical yield ranged from 20% to 100% but, for each analytical batch, the highest yield ranged from 80% to 100%. Therefore, we considered a chemical yield of 90% ± 10% to the samples of stations S1 and S2 with the highest count rate of ^{233}Pa and deduced the concentration of the spike solution by using the sensitivity (count per second per ppt) measured on a ^{231}Pa-^{233}U calibration solution. This procedure was checked on stations S3, S4 and S5, the concentrations deduced for all samples fall within ± 10% of concentrations deduced from the true spike concentration obtained by the spike calibration against the home standard.

^{231}Pa concentrations were corrected for ingrowth from ^{235}U decay between the on-board sampling and the U-Pa chemical separation (Levier et al., 2021). All uncertainties were propagated through signal processing equation and correction equation, and each of them was expressed with a confidence interval of 95% (2 times standard error: $2\sigma_n$).

2.5. Lithogenic contribution correction

To consider exclusively ^{231}Pa concentration produced *in situ* by the ^{235}U decay, the ^{231}Pa concentrations measured by mass spectrometry were corrected from the contribution brought by lithogenic material, where we used ^{232}Th as a proxy. The excess of ^{231}Pa was expressed as follows:

$$^{231}Pa_{xs} = {}^{231}Pa_m - {}^{232}Th_m \times \left(\frac{^{238}U}{^{232}Th}\right)_{litho} \times \left(\frac{M_{231}}{M_{232}}\right) \times \left(\frac{\lambda_{232}\times\lambda_{235}}{\lambda_{238}\times\lambda_{231}}\right) \times \left(\frac{^{235}U}{^{238}U}\right)_{nat} \quad (1)$$

Where $^{231}Pa_{xs}$ is the excess of ^{231}Pa corrected from the lithogenic contribution expressed here in fg/kg, $^{231}Pa_m$ and $^{232}Th_m$ are the measured isotopes (Roy-Barman et al. 2019) respectively expressed in fg/kg and in pg/kg. λ_{232}, λ_{231}, λ_{235} and λ_{238} are the decay constant of ^{232}Th, ^{231}Pa, ^{235}U and ^{238}U respectively. M_{231} and M_{232} are the molar masses of the ^{231}Pa and ^{232}Th. $(^{235}U/^{238}U)_{nat}$ is abundance ratio between natural uranium isotopes, here 1/137.818 mol/mol (Livermore et al., 2018, Condon et al., 2010). The mean crustal activity ratio $(^{238}U/^{232}Th)_{litho}$ =

204 0.4 ± 0.1, estimated south of the Antarctic Polar Front (Rutgers van der Loeff and Berger, 1993;
205 Venchiarutti et al., 2011).

206 3. Results

207 Dissolved Protactinium-231 corrected from the lithogenic contribution ($^{231}Pa_{d\text{-}xs}$) measured for
208 the Bonus GoodHope cruise ranged from 0.33 ± 0.04 µBq/kg (1µBq/kg = 0.5676fg/kg = 0.06
209 dpm/m^3) in surface water to 6.09 ± 0.11 µBq/kg (Table ES1) in bottom water with a general
210 increase with depth (Fig. 2). From station S1 to S3, we observe a similar profile with a
211 quasi-linear increase from the surface to around 1500m. At Station S1, we see a maximum
212 concentration of 5.88 ± 0.11 µBq/kg at 3000m, in NADW, and decrease to 4.91 ± 0.11 µBq/kg
213 at 4000m in the AABW. At station S3, there is a sharp decrease of the concentration, from 4.85
214 ± 0.09 µBq/kg at 3000m to 2.92 ± 0.07 µBq/kg in the bottom water. This decrease was already
215 noted for dissolved REE (Garcia Solsona et al., 2014) and thorium isotopes (Roy-Barman et al.,
216 2019). Processes that could account for the observed near-bottom decrease include enhanced
217 scavenging onto particles of hydrothermal origin or onto particles originating as nepheloïd
218 layers.

219 The Bonus GoodHope cruise occurred 3 weeks after the ZeroDrake cruise, where the
220 Greenwich meridian was also sampled across the ACC for $^{231}Pa/^{230}Th$ studies (Rutgers van der
221 Loeff et al., 2016; Venchiarutti et al., 2011). Thorium isotopes were consistent between the two
222 cruises (Roy-Barman et al., 2019). Consistent data are also obtained for $^{231}Pa_{xs,}$ when we
223 compare stations S2 to S4 with nearby ZeroDrake stations (Fig. ES1). At these stations, the
224 BGH concentrations tend to be on the low side of the Drake values. However, an
225 intercalibration exercise between LSCE and AWI, on strictly identical samples, proved an
226 agreement within a few percent for ^{231}Pa measured in deep arctic sample (Gdaniec et al in prep).
227 By contrast, in the Weddell Gyre, the dissolved $^{231}Pa_{xs}$ was almost twice less concentrated at
228 Station S5 compared to station 131 of the ZeroDrake cruise. There is about 150 km between
229 these stations (0.00E, 57.5S for the BGH sampling point and 0.00E, 59.0S for the ZeroDrake
230 one). Possible reasons for this discrepancy will be discussed in section 4.1.

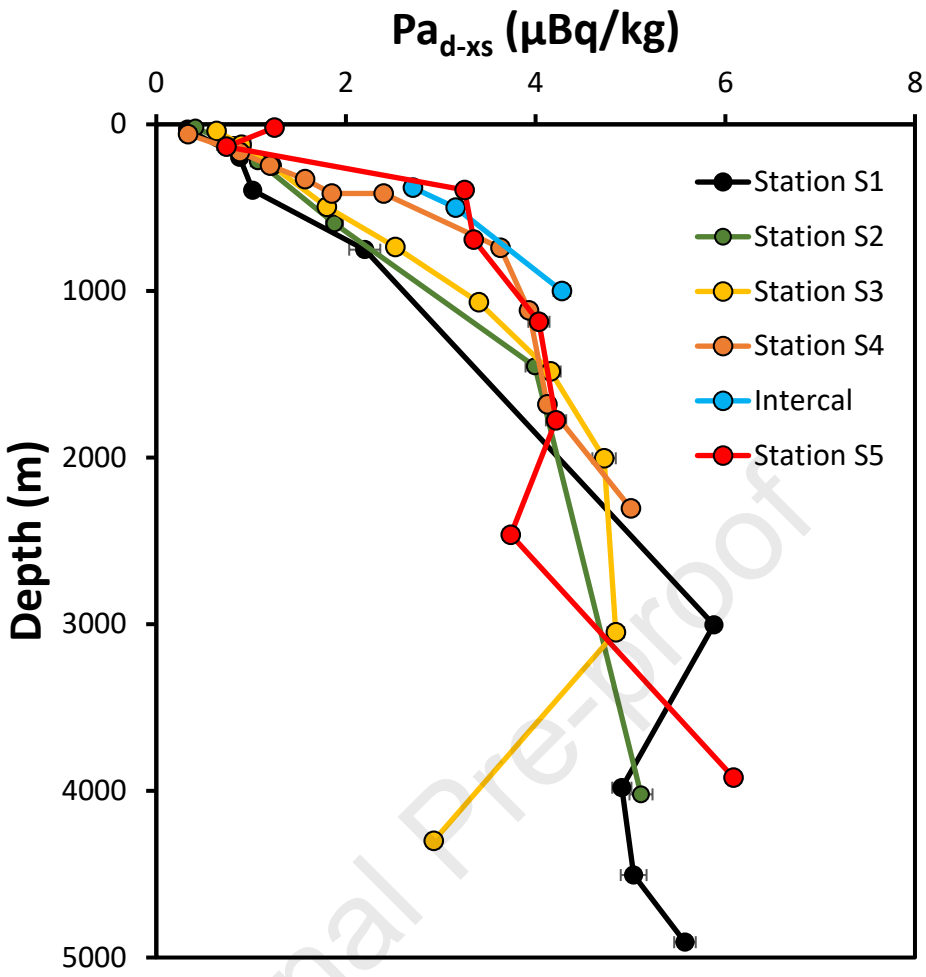

231

Figure 2 : $^{231}Pa_{xs}$ concentration in the dissolved phase of the super stations of the Bonus GoodHope cruise

232

233 The excess ^{231}Pa concentration of the particulate fraction ($^{231}Pa_{p-xs}$) range from 0.0014 ± 0.0003
234 µBq/kg in surface water (station S4) to 0.573 ± 0.092 µBq/kg in bottom water of station S1
235 (Fig. 3). The $^{231}Pa_{p-xs}$ concentrations are rather constant through the water column with a sharp
236 increase near the seafloor, except at station S3, where the deepest concentration remains similar
237 to the intermediate waters (Table ES2).

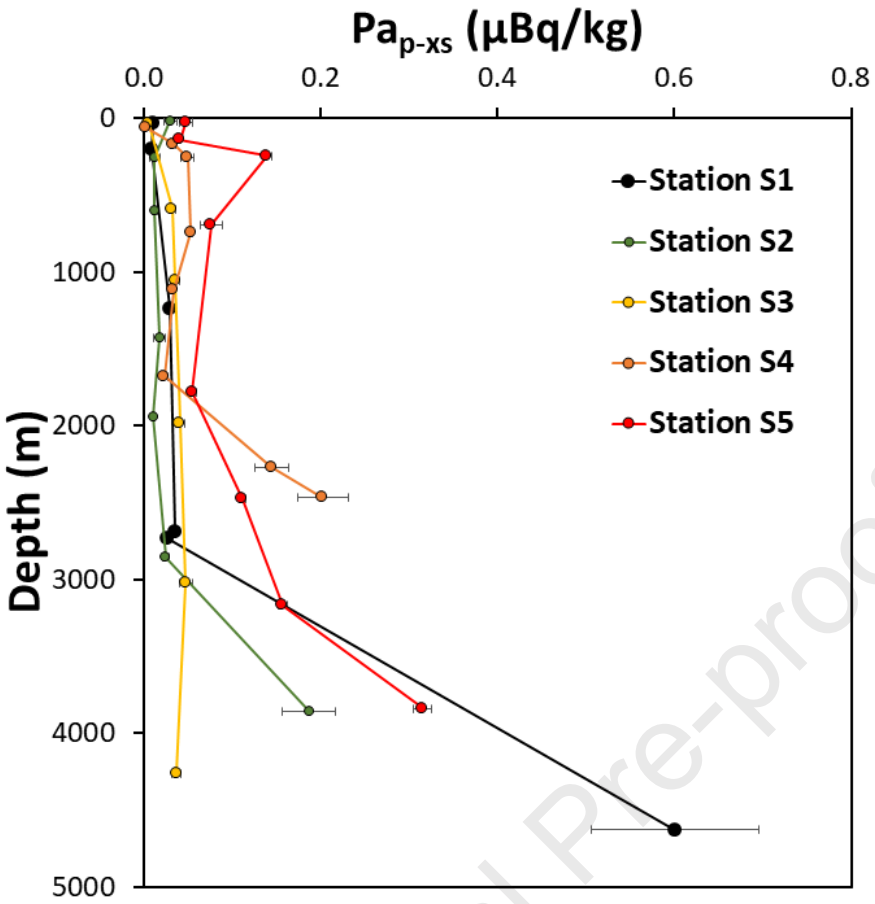

Figure 3 : $^{231}Pa_{xs}$ concentration in the particulate phase of the super stations of the Bonus GoodHope cruise

4. Discussion

4.1. Dissolved ^{231}Pa in the Weddell Gyre

Dissolved ^{231}Pa profiles are variable in the Weddell Gyre (Rutgers van der Loeff et al., 2016). The cyclonic circulation in the Weddell isolates an inner zone with high $^{231}Pa_{d-xs}$ concentrations (up to 9.69 ± 0.55 µBq/kg, at station 131 of Rutgers van der Loeff, 2016) whereas the rim has lower concentrations (about 7.30 ±0.90 µBq/kg, at station 161 of Rutgers van der Loeff, 2016). The reasons for this concentration gradient are unclear. The low dissolved $^{231}Pa_{xs}$ measured at Station S5, is in line with the peripheral location of the station in the gyre at the boundary between the Weddell gyre and the southern area of the ACC. This region has a strong gradient, with an enriched concentration in the Weddell gyre compared to the ACC, for several radioactive isotopes like ^{230}Th, ^{232}Th, ^{231}Pa (Rutgers van der Loeff et al., 2016; Venchiarutti et

al., 2011) or Pb (Boye et al., 2012).

Station S5 and station PS63-161 of ANT-XXIV/3 cruise located 150 km further south show a strong difference in $^{231}Pa_{xs}$ concentration despite being in the same hydrological settings (Fig. 4). Several causes have been investigated to explain the large $^{231}Pa_{xs}$ offset observed between the two stations. Firstly, we have carefully checked the data, from the possible biases of the analytical process, like Pa adsorbtion on stock bottle, to the data processing. However, station S5 samples have been processed in the same analytical batch as the ones from station S4, which is in good agreement with concentrations measured at station 131 of ANT-XXIV/3 cruise (Fig ES1). Secondly, like the strong $Pa_{d\text{-}xs}$ gradient is not an analytical bias, we looked for the processes leading to such gradient.

The WSDW is newly formed deep water in the Weddell Sea, reflected by its highly oxygenated signature (about 250 µmol/L). The dissolved oxygen in bottom water of station S5 (O_2 = 248.3 µmol/kg, (Branellec et al., 2010) is higher than at ZeroDrake station 131 (O_2 = 241.7 µmol/kg) (Fahrbach & Baar, 2010), suggesting a younger water at station S5 (Fig. ES2). Assuming an oxygen utilization rate (OUR) of about 0.12 - 0.14 µmol/L/y (Broecker et al., 1991; Feely et al., 2004), it would take about 50 y to produce the observed O_2 deficiency of ~7 µmol/L observed at station 131. We note a $^{231}Pa_{d\text{-}xs}$ difference between the stations S5 and 131of about 3.5 µBq/kg. This offsetwould take about 80 y to build up by *in situ* ^{235}U decay production (~ 0.044 µBq/kg/y). Such period is consistent with the age difference calculated from oxygen data.

Neodymium isotopes also support the occurrence of several water masses in the deep water at stations S5 and 131. There is a significant difference (1 epsilon unit) of the Nd signature of deep water from station S5 (-10 ± 0.4 at 3900 m and -10.1 ± 0.5 at 3150 m) (Garcia-Solsona et al., 2014) and 131 (around -9.5 ± 0.3 at 3900 m and -9 ± 0.5 at 3000 m) (Stichel et al., 2012). The Nd signature at station S5 highlights an imprint of the Weddell shelf sediment signature (ε_{Nd} = -15 ; Robinson et al., 2021) on the incoming WDW (ε_{Nd} = -9.5 at 3000 m at station 161 Stichel et al., 2012a). In contrast, the signature at station 131 reflects the larger fraction of the incoming CDW (ε_{Nd} = -8.4) (Amakawa et al., 2019) in the water recirculating in the Weddell gyre (ε_{Nd} = -10).

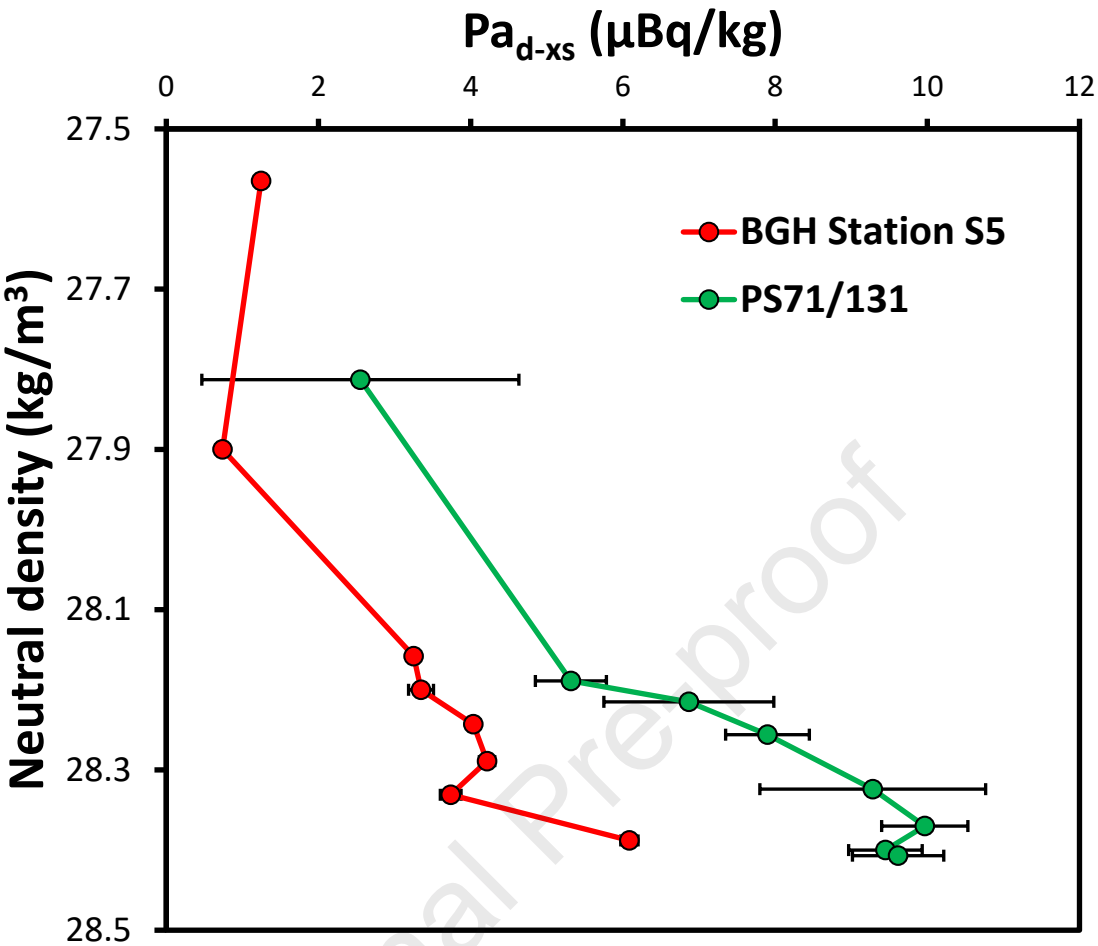

Figure 4 : $^{231}Pa_{xs\text{-}total}$ versus neutral density in the Weddell gyre during the Bonus GoodHope and ZeroDrake cruises. Red : station S5 BGH; green: station 131 of ZeroDrake cruise

4.2. ^{231}Pa dissolved/particles partition

^{231}Pa and ^{230}Th have different affinities for the different phases of marine particles. This leads to a significant offset between the *in situ* production ratio and the measured ones in dissolved, particulate and sediment phases. To identify which water masses contribute to the Pa accumulation in seawater, we usually use the fractionation factor ($F_{Th/Pa}$) defined as :

$$F_{Th/Pa} = \frac{K_d(Th)}{K_d(Pa)} = \frac{\left(\frac{^{231}Pa_{xs}}{^{230}Th_{xs}}\right)_{diss}}{\left(\frac{^{231}Pa_{xs}}{^{230}Th_{xs}}\right)_{part}} \qquad (2)$$

Where K_d represent the partition coefficient between dissolved and particulate phases respectively for Th and Pa. Thorium data were measured on the same seawater samples as ^{231}Pa

(Roy-Barman et al., 2019). $F_{Th/Pa}$ across the ACC range from 0.57 ± 0.06 in shallow water of the station S5 to 37.6 ± 16.2 at 1450 m depth at station S2 (Fig. 5; Table ES2). We observe a meridional gradient of $F_{Th/Pa}$, from over 20 in the north of the ACC to below 1 south of the polar front. This values and gradient are consistent with previous observations (Chase et al., 2002; Venchiarutti et al., 2011; Walter et al., 1997), highlighting the sink of dissolved Pa south to the polar front.

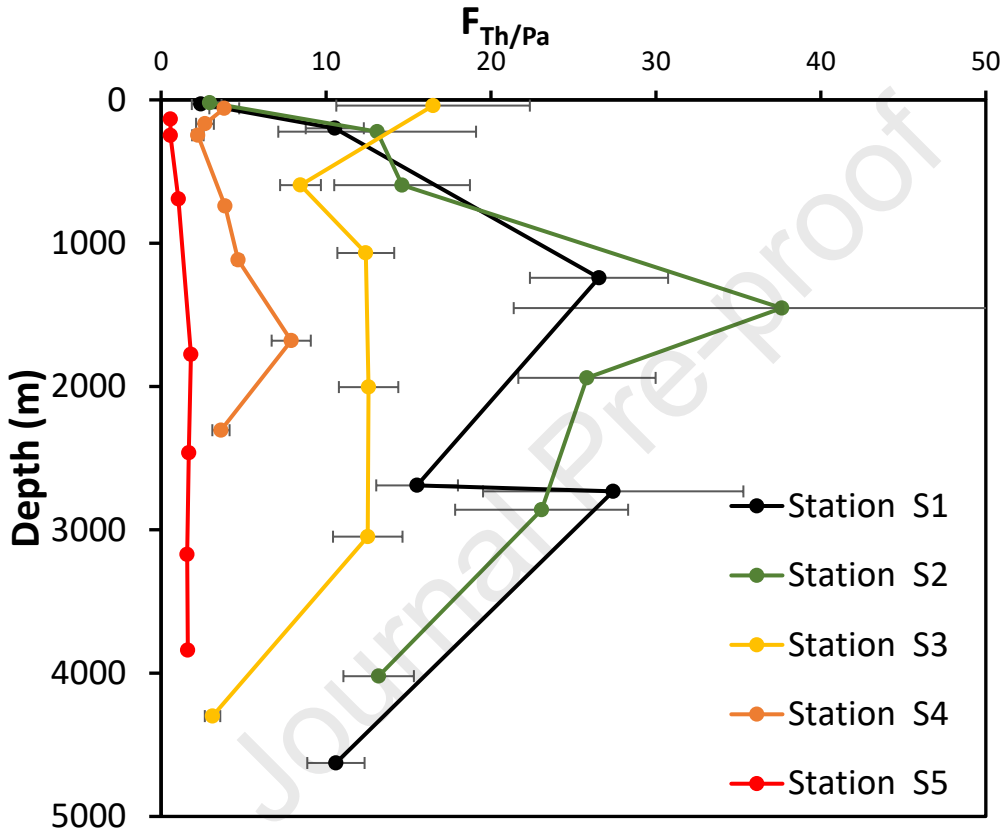

Figure 5 : $F_{Th/Pa}$ fractionation factor profiles. The dissolved concentration was interpolated linearly between two points measured on neutral density basis at depths where particulate concentration was measured. $F_{Th/Pa}$ uncertainties are propagated and expressed in $2\sigma_n$

The $F_{Th/Pa}$ is a proxy of the relative Pa accumulation in dissolved water compare to the ^{230}Th that is efficiently accumulated in particulate fraction (Hayes et al. 2015). So we observe an increase of the the ^{231}Pa/^{230}Th from the north to the South of the ACC, like expected in the AMOC hypothesis of Pa/Th distribution. However, $F_{Pa/Th}$ show a strong shift on the Pa/Th burial dynamic by crossing the ACC. By crossing the ACC, the phytoplanctonic activity shift of prevailing species, which modify the marine particle composition, with here the presence of diatoms of the Opal Belt (Chase et al., 2002 ; Walter et al., 1997).

Although the ^{231}Pa high affinity for opal is commonly admitted, its magnitude remained roughly known. This limit further modelling applications to assess the Pa/Th ratio as a paleo proxy of deep water ventilation or particles composition. We use this new dataset to propose a new estimation of ^{231}Pa partition coefficient on suspended opal. The partition coefficient is the concentration adsorbed on particles normalized by to the dissolved concentration (Hayes et al., 2015):

$$K_{d-bulk}(X) = \frac{X_{ads}}{X_{diss}} \times \frac{1}{SPM} = \frac{\frac{X_{ads}}{SPM}}{X_{diss}} \quad (3)$$

Where X represents ^{231}Pa or ^{230}Th, in the adsorbed (~ particulate concentration) and dissolved fractions, and SPM the mass of suspended particle matter in seawater that we calculated as the sum of the opal, carbonate, particulate organic matter (POM) and lithogenic matter. The opal mass in particle matter in estimated from the BSi concentration (Fripiat et al., 2011) with the mean opal molar mass (SiO_2,0.4(H_2O)). The carbonate ($CaCO_3$) concentration was estimated from the particulate Ca concentration (Table ES3). POM mass was approximated from the particulate organic carbon (POC) (Cavagna et al., 2013) with POM = 2 × POC (Winogradow et al., 2019). The lithogenic matter was approximated from the ^{232}Th particulate concentration (Roy-Barman et al., 2019) with ^{232}Th concentration in lithogenic matter is about 10 ppm.

$K_{d\text{-}bulk}$(Pa) and $K_{d\text{-}bulk}$(Th) were calculated for samples where BSi concentrations were available. The $K_{d\text{-}bulk}$(Pa) range from 0.062 to 2.79 $\times 10^6$ g/g, and $K_{d\text{-}bulk}$(Th) range from 0.212 to 9.92 $\times 10^6$ g/g . ^{231}Pa concentration is assumed to be mainly driven by the biogenic opal biogeochemical cycle at high latitudes, but there is a weak correlation between the $K_{d\text{-}bulk}$(Pa) of Bonus particles and the BSi proportion of marine particles (R^2 = 0.17). There is also no correlation with the $K_{d\text{-}bulk}$(Th) (R^2 = 0.02) (Fig. ES3). Although we expected a strong affinity of Pa toward opal phase, other bearing phases have to be considered. So, by subtracting the contributions from these other phases, we deduce K_{d_opal}(Pa), the specific partition coefficient for the opal phase (Hayes et al., 2015)

$$K_{d-opal} = \frac{(K_{d-bulk} - f_{litho} \times K_{d-litho} - f_{CaCO3} \times K_{d-CaCO3} - f_{POM} \times K_{d-POM})}{f_{opal}} \quad (4)$$

Where f_{litho}, f_{CaCO3}, f_{opal} and f_{POM} are the mass fractions of each phase in particles, $K_{d\text{-}litho}$, $K_{d\text{-}CaCO3}$ and $K_{d\text{-}POM}$ are the partition coefficient of each phase, with respective values : 2.3 $\times 10^6$; 0.9 $\times 10^6$ and 0.2 $\times 10^6$, determined on North Atlantic particles (Hayes et al., 2015). We consider

only particulate samples containing more than 50% of BSi (samples from opal belt and south of the polar front) to minimize the impact of other phases and so limiting the uncertainty amplification from BSi-poor samples. we obtain $K_{d\text{-}opal}(Pa) = 1.42 \pm 0.55 \times 10^6$ g/g (1 standard error). $K_{d\text{-}opal}(Th)$ calculated in the same way does not provide a significant value. We assume that Th affinity for the prevailing opal phase is weak against the contribution from the strong affinity on other phases.

$K_{d\text{-}opal}(Pa)$ rough estimation on suspended particles are in the upper range of previous estimation made on sediment trap material ($K_{d\text{-}opal}(Pa)$ = 1.0 to 1.4× 10^6 g/g, Chase et al., 2002; Li, 2005; Luo and Ku, 2004), and over the estimation made on SiO_2 from diatoms in laboratory experiment ($K_{d\text{-}opal}(Pa) = 1.9 \times 10^5$ g/g, Lin et al., 2014 ; $K_{d\text{-}opal}(Pa) = 5.0 \times 10^5$ g/g Geibert and Usbeck, 2004). Our new value confirms the opal affinity is stronger for *in situ* materials than laboratory controlled one. This discrepancy should result from the difference in opal state. The first laboratory experiment made a chemical digestion to remove organic matter from oceanic diatoms frustules (Geibert et Usbeck, 2004). The second experiment was perfomed on silica nanoparticles (Lin et al., 2014). In these two experiments, they didn't study the impact of the organic matter contribution on the partition coefficient of opal. The gradual dissolution of opal matter could also contribute to this difference. The dissolution affect organic matter but also the opal surface configuration, modifying the ratio adsorption site over opal mass. This second assumption leads to a variable $K_{d\_opal}(Pa)$ parameter in water column.

4.3. Isopycnal transport and scavenging of ^{231}Pa across the ACC

Across the ACC, ^{230}Th concentrations were shown to be relatively conservative along isopycnal surfaces (Roy-Barman et al., 2019; Rutgers van der Loeff and Berger, 1993). Thorium isotopes transport along the BGH section was represented with an advection-diffusion-scavenging model along isopycnal surfaces, with solution parameters reported in Table 1. The transport was assumed to be the residual meridional component of the mixing from advection and diffusion) embedded in the dominant zonal circulation. This allowed linking tracers (θ-S-^{230}Th-^{232}Th) and estimating transport parameters (Roy-Barman et al., 2019). Seawater ^{231}Pa content is constrained by the same fluxes as Th isotopes : (1) the *in situ* production from uranium decay; (2) the removal by adsorption on settling particles; (3) the advection of water masses; (4) the eddy diffusion which we assume no impact of the diapycnal component (illustrated in

364 Fig. 6).Then, we apply the advection-diffusion-scavenging model on ^{231}Pa from BGH cruise to
365 test the robustness of the model and refine the transport parameter estimations.

366 As for Th isotopes, we focus on two isopycnal surfaces defined by γ_n = 27.865 kg/m^3 and γ_n =
367 28.094 kg/m^3 (Fig. 7). The first isopycnal surface (γ_n = 27.865 kg/m^3) links the I-UCDW (Indian
368 Upper Circumpolar Deep Water) at station S1 (1500 m) to the D-UCDW (Drake Passage Upper
369 Circumpolar Deep Water) at station S4 (200 m). The second isopycnal surface (γ_n = 28.094
370 kg/m^3), in the southern part of the ACC, links the upper part of the NADW at the station S3
371 (2500 m) to the WDW at station S5 (150 m). These two isopycnal surfaces were chosen because
372 along the Bonus Good Hope section they best correspond to a two water masses mixing as
373 indicated by θ-S data.

374

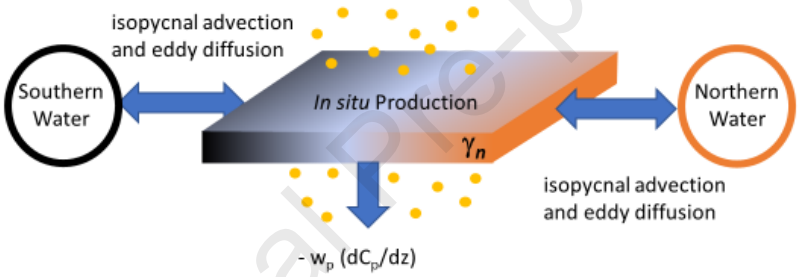

375

Figure 6 : Conceptual diagram of the advection-diffusion-scavenging model

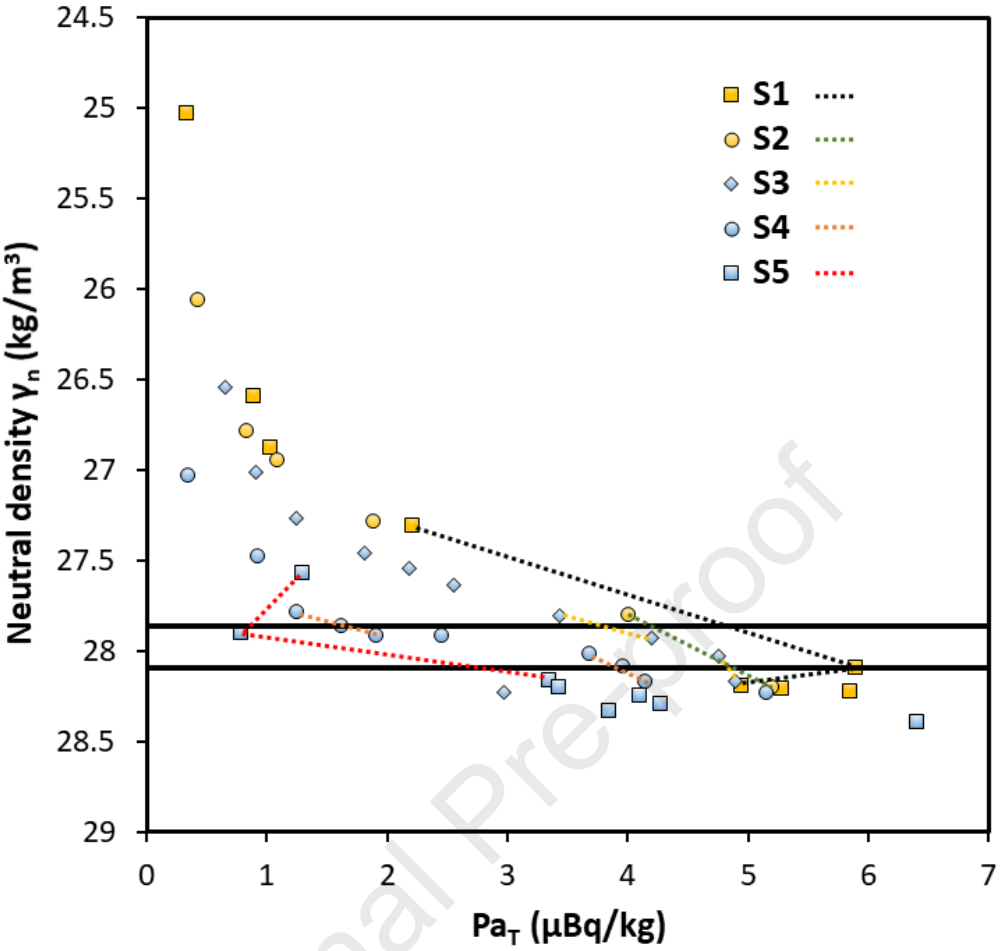

376

Figure 7 : Distribution of the $^{231}Pa_T$ (Pa_d + Pa_p) concentration from the Bonus GoodHope cruise against the neutral density. The studied isopycnal surfaces (γ_n = 27.865 kg/m^3 and γ_n = 28.094 kg/m^3) are highlighted by black lines. Blue point are measurement from stations at high latitudes (S3, S4, S5) and yellow one from lower latitudes (S1, S2). Dashed lines represent the linear interpolation to determine the Pa_T concentration at the isopycnal surface.

377

378 Assuming steady state, the transport equation along an isopycnal surface (Roy-Barman et al.,
379 2019) is given by :

380
$$K_i \frac{\partial^2 C_t}{\partial x^2} - u_i \frac{\partial C_t}{\partial x} + P_d - w_p \left(\frac{\partial C_p}{\partial z} \right) = 0 \quad (5)$$

381 Where K_i and u_i are respectively the cross-stream (meridional component) eddy diffusion
382 coefficient and the cross-stream advection velocity coefficient over the studied isopycnal
383 surface. P_d is the *in situ* production of the radiogenic element and w_p the settling speed of
384 particles. C_t and C_p are respectively the total concentration and the particulate concentration of
385 the radiogenic element.

386 The x-axis is parallel to the isopycnal surface in the meridional direction and oriented northward.
387 The z-axis is oriented perpendicular to the isopycnal surface and hence is almost vertical. Just
388 like in the reversible scavenging model, keeping w_p out of the partial derivative requires to
389 assume that w_p does not vary with z. The Eq. (5) was integrated along the isopycnal surface of
390 the BGH section between the stations corresponding to the end members of water mass mixing
391 (stations S1 and S4 for γ_n = 27.865 kg/m^3, from the I-UCDW to the DP-UCDW and S3 and S5
392 for γ_n = 28.094 kg/m^3, from the NADW to the WW). This is a simplified view of water transport
393 because while water moves across the ACC, it is also rapidly advected eastward by the ACC
394 (S2–S4) and the northern limb of the Weddell Gyre (S5). We assume that K_i, u_i, w_p and (dC_p/dz)
395 are all constant along x in order to obtain analytical solution. We note C_t=$C_{t\text{-}cons}$ + ΔC_t, where
396 $C_{t\text{-}cons}$ is the concentration of the tracer if it behaves as a conservative mixing (only mixing by
397 advection and diffusion) and ΔC_t is the deviation of this tracer due to the radioactive production
398 and scavenging on settling particles. By analogy with Roy-Barman study, the solution is then:

399 $$C_{t-cons} = \frac{e^{\frac{u_i}{K_i}x} - e^{\frac{u_i}{K_i}x_B}}{e^{\frac{u_i}{K_i}x_A} - e^{\frac{u_i}{K_i}x_B}}\left(C_{t\_A} - C_{t\_B}\right) + C_{t\_B} \quad (6)$$

400 $$\Delta C_t = \frac{\left(P_d - w_p \frac{dC_p}{dz}\right)}{u}\left((x - x_B) + (x_B - x_A)\left(\frac{e^{\frac{u_i}{K_i}x} - e^{\frac{u_i}{K_i}x_B}}{e^{\frac{u_i}{K_i}x_A} - e^{\frac{u_i}{K_i}x_B}}\right)\right) \quad (7)$$

401 Where the suffixes A and B represents the end-member stations (respectively S1 and S4) and x
402 the latitudinal position. For a conservative tracer such as the salinity (S), the concentration is
403 given by:

404 $$S = \frac{e^{\frac{u_i}{K_i}(x-x_A)} - 1}{e^{\frac{u_i}{K_i}(x_B-x_A)} - 1}(S_B - S_A) + S_A \quad (8)$$

405 This equation allows to determine $u_i/K_i \approx$ -1.6 10^{-6} m^{-1} for both isopycnal surfaces (Roy-
406 Barman et al., 2019), the negative value means a southward advection, K_i is always positive
407 and diffusive flux orientation depends of the concentration gradient, here it is a southward flux.
408 Then these equations were applied to ^{230}Th and ^{232}Th to derive a first estimate of the transport
409 parameters (Table 1, see Roy-Barman et al., 2019 for details of the calculations). By analogy,
410 we applied these equations to ^{230}Th and ^{232}Th and ^{231}Pa data of the BGH cruise to obtain a
411 second set of transport parameters. As Th isotope total concentration, the Pa_T concentrations at

412 isopycnal surfaces are defined by a linear interpolation on the neutral density scale (Fig. 7) and
413 the relative uncertainties were chosen as the same as the widest one among the interpolation
414 points of each station.

415 We use a Monte-Carlo simulation (n=50000) over the three model parameters (u_i, K_i, w_p) with
416 a large dispersion of the their a priori values. The dC_p/dz a priori value is defined as the average
417 of particulate gradients measured perpendicular to the isopycnal surface, on station linked to
418 this isopycnal surface, and we assigned an uniform dispersion covering a range wider than data
419 (from 10^{-6} to 10^{-3} µBq/kg/m). As determined before, we constrain u_i and K_i so that u_i/K_i ratio
420 remains the solution of the conservative equation. For each simulation n, we determined the
421 coefficient of determination ($R^2_n(X)$) of the simulated mixing curves and measured data of ^{231}Pa,
422 ^{230}Th and ^{232}Th. From these three $R^2_n(X)$, we calculated a mean R^2_n to which one we apply a
423 selection filter. We arbitrarily put the selection at $R^2 = 0.97$ for the first isopycnal surface (γ_n =
424 27.865) and $R^2 = 0.75$ for the second one (γ_n = 28.094). We save the input parameter values for
425 each selected mixing curve. De facto, only the most fitting quartet of simulated parameters are
426 retained over the n simulations. The quartet parameter which are solution of the equations
427 follow a normal distribution, so we choose as mean value the average of the selected parameter
428 with one standard deviation as uncertainty. The mean values and uncertainties are reported in
429 Table 1, with the values obtained previously with only thorium isotopes (Roy-Barman et al.
430 2019). Model results are displayed in figure 8, predicting an almost linear Pa distribution
431 between the end-members stations. This prediction is in good agreement with BGH data.

432 Including ^{231}Pa in the model, there is no significant change on the average estimation of the
433 parameter K_i and u_i values, but the uncertainties are reduced by a factor 2 to 4 (Table 1). Among
434 the model parameters, the particle settling speed is the most affected by the introduction of the
435 Pa constraints. It provides higher settling speed on the isopycnal surface 27.865 kg/m^3, with a
436 value of 990 ± 85 m/y against 674 ± 250 m/y with Th isotopes alone (Table 1). This change of
437 settling speed occurs on the sloped isopycnal surface which cross the whole ACC. So, this
438 isopycnal surface follows the particle composition evolution along the BGH transect, reflected
439 by the $\frac{d^{231}Pa_p}{dz}$ variations ranging from 10^{-6} to 10^{-4} µBq/kg/m. Conversely, calculation on the
440 other isopycnal surface (γ_n = 28.094 kg/m^3) is based more on the southern stations, with a steady
441 particle composition. Therefore, the addition of ^{231}Pa data in the isopycnal advection-diffusion-
442 scavenging model provide consistent transport parameter estimations, and provides significant
443 diminution of the solutions dispersion (Tab. 1).

Table 1 : Model parameters and output, x-axis is oriented northward

γ_n (kg/m^3)	d^{231}Pa$_p$/dz (µBq/kg/m)	K_i (m²/s)	u_i (m/s)	w_p (m/y)	Best fit R^2 ^{232}Th	Best fit R^2 ^{230}Th	Best fit R^2 ^{231}Pa
Roy-Barman et al. (2019)							
27.865 (S1-S4)	--	2000 ±840	- 0.0033 ± 0.0014	674 ±250	0.994	0.945	
28.094 (S3-S5)	--	2180 ±480	- 0.0036 ± 0.0008	418 ±470	0.696	0.806	
This study							
27.865 (S1-S4)	6.5e-6 ±3.3e-6	1900 ±180	- 0.0030 ±0.0003	990 ±85	0.994	0.945	0.997
28.094 (S3-S5)	4.4e-4 ±4.0e-4	1900 ±120	- 0.0031 ±0.0002	370 ±200	0.0696	0.806	0.922

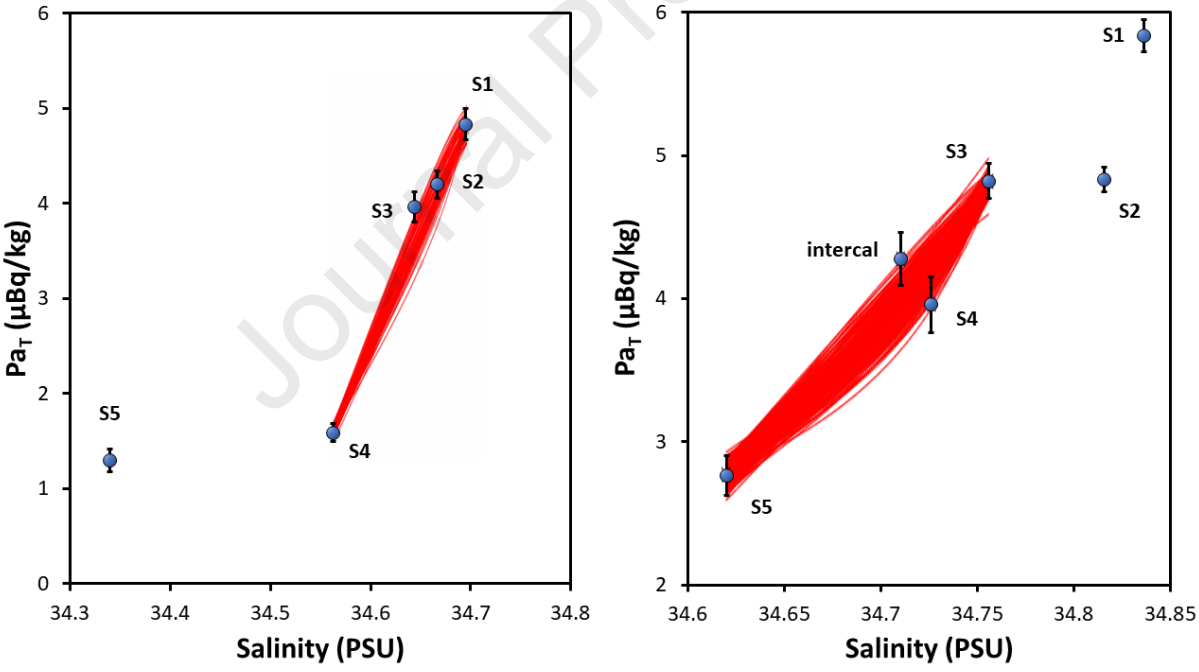

Figure 8 : Advection-diffusion modelling of Salinity and $^{231}Pa_T$ compared to data, at the isopycnal surface γ_n= 27.865 kg/m^3 (a) and at the isopycnal surface γ_n= 28.094 kg/m^3 (b). Stacked red curves are the fitting curved with the best R² obtained with the Monte Carlo simulation.

We use a box model to evaluate the weight of each ^{231}Pa transport flux relative to the in situ production. For each isopycnal surface, the box model is bounded to north and south by their respective end-member stations. Horizontal length L is the distance between the two end-

member stations. The width l and the height h of the box don't appear in final equation. We linearly extrapolate the ^{231}Pa concentrations at the depth where the isopycnal surface is located to calculate the horizontal gradient. The vertical gradient $\frac{d^{231}Pa_p}{dz}$ is an average value at the depth of the isopycnal surface (γ_n = 27.865 kg/m3 and γn = 28.094 kg/m3) on respectively stations S1-S4 and stations S3-S5. The *in situ* production rate in seawater is constant P = 44 µBq/kg/y. Transport parameters are the mean solutions provide by the advection-diffusion-scavenging model. The values apply in the box model are summarized in table 2. Weighted flux contributions are respectively expressed:

$$\frac{\Phi_{diff}}{\Phi_{prod}} = \frac{\frac{d^{2231}Pa_d}{dx^2} \times K_i}{P} = \frac{K_i \times (Pa_i - Pa_o)}{P \times L^2} \quad (9)$$

$$\frac{\Phi_{adv}}{\Phi_{prod}} = \frac{u_i \times \frac{d^{231}Pa_d}{dx}}{P} = \frac{(Pa_i - Pa_o) \times u_i}{P \times L} \quad (10)$$

$$\frac{\Phi_{scav}}{\Phi_{prod}} = \frac{w_p \times \frac{^{231}Pa_p}{dz}}{P} \quad (11)$$

At the isopycnal γ_n = 27.865 kg/m3, the ^{231}Pa inflowing from the I-UCDW represents 4.13 times the in situ production (Tab. 2). We also observe the diffusive flux is an important inflow of ^{231}Pa to the Southern Ocean ($\frac{\Phi_{diff}}{\Phi_{prod}} = 1.55$). These large Pa influxes are consistent with Pa budget previously published (Rutgers van der Loeff et al., 2016). However, the Pa scavenging flux observed does not balance the isopycnal surface Pa budget ($\frac{\Phi_{scav}}{\Phi_{prod}} = 0.15$). Pa scavenging is particularly low at this isopycnal surface compared to previous measurements in the ocean made from the whole water column. However, estimate of the particle fall velocity is of the same order of magnitude as those obtained by Th isotopes (Roy-Barman et al. 2019). Then, the flux intensity depends on the particle Pa gradient measured on the isopycnal surface, which ranges from 10^{-6} at station S1 to 10^{-4} at station S4. This meridional gradient is also noted in the meridional evolution of the Pa_p/Pa_d ratio, ranging from 0.5% in the north to 4% in the south of the ACC (Tab. ES2), strongly constrained by the particles composition and in particular the biogenic silica.

In the same way, we calculate the ^{231}Pa budget of the second isopycnal surface (γ_n = 28.094 kg/m^3), connecting the ACC to the Weddell gyre. The scavenging flux represents here 3.40 times the in situ production, consistent with previous opal belt scavenging efficiency. However, it remains weaker than northern cumulated inputs from advection ($\frac{\Phi_{adv}}{\Phi_{prod}} = 4.63$) and diffusion ($\frac{\Phi_{diff}}{\Phi_{prod}} = 2.58$), leading to a budget also unbalanced.

These Pa budgets are made on the isopycnal surface and should not be extrapolated to the whole ACC. First, Pa advection is driven by water mass circulation. In the model, the isopycnal is located in the southward flowing deep water (UCDW and NADW), while intermediate (AAIW) and bottom water (AABW) flow northward (Abadie et al., 2016). Secondly, it is a rough approximate to consider a homogeneous particle fall, at a constant velocity through the whole transect and water column. Most of the Sourthern Ocean particle are produced by the biological activity, and are gradually degraded as they fall by the remineralization. The degradation of the particles decreases their size and alter their settling speed velocity. Thirdly, this degradation could also modify the adsorption site available for Pa, by enhancing the adsorption area or enhancing Pa desorption by substrate dissolution. This should results to a partitioning coefficient variation through the water column. Another limit of the budget at the isopycnal surface γ_n = 27.865 kg/m^3 is the relative weight of the ACC area against the opal belt one. The budget is built to connect the isopycnal surface from the station S1 to the station S4, so almost all the ACC area is considered while only the northern part of the opal belt is considered. This lead to underestimate the average scavenging flux of the whole ACC. Finally, the parameters are extract of a purely meridional model, so the mean zonal circulation was neglected which transport Pa to the Inadian section of the Southern Ocean (Rutgers van Der Loeff et al., 2016).

Table 2 : Box-model parameters used and weighted flux contribution on Pa budget

	γ_n = 27.865 kg/m3	γ_n = 28.094 kg/m3
L (m)	1690000	1100000
P (µBq/m^3/y)	44	44
u_i (m/s)	0.0030	0.0031
K_i (m²/s)	1900	1900
w_p (m/y)	990	340
$^{231}Pa_i$ (µBq/m^3)	4830	4800
$^{231}Pa_o$ (µBq/m^3)	1590	2500
$d^{231}Pa_p/dz$ (µBq/m^3/m)	0.0065	0.44
$\frac{\Phi_{adv}}{\Phi_{prod}}$	4.13	4.63
$\frac{\Phi_{diff}}{\Phi_{prod}}$	1.55	2.58
$\frac{\Phi_{scav}}{\Phi_{prod}}$	0.15	3.40

5. Conclusion

This study constitutes a new step in the understanding of the Pa cycle and the influence of the particle composition in its scavenging flux. We have demonstrated our ability to produce data in good agreement with those obtained by other research teams, on waters sampled close in time and space. A significant offset is highlighted in the Weddell gyre, attributed to an age difference of about 80 years between the WSW from two points of its cyclonic circulation. We also calculate a new value of the partition coefficient of Pa on biogenic silica, thanks to the coupled study of Pa and the elements constituting the marine particles. This estimate reinforces those obtained on sediment-traps but is higher than the ones obtained in laboratory experiments. Lastly, the addition of Pa to the advection-diffusion-scavenging model does not affect the solutions of the transport parameters determined with Th isotope, but this new constraint reduces their uncertainties. To improve ACC meridional mixing comprehension, the addition of other radiochronometer is possible, such as ^{227}Ac or ^{228}Ra, to bring new constraints or to consider other processes such as diapycnal mixing. However, the transport parameters remain linked the isopycnal surface, and then be extrapolate to the water mass only. Pa data also show a weak Pa scavenging in the UCDW, reflected by the very low concentration in the particulate phase compared to the dissolved one.

We note that advection-diffusion-scavenging model is based on the hypothesis of a

517 homogeneous particle flux along the isopycnal surface. This hypothesis is not verified but we
518 still apply an average particular flux to remain in the application scope of the model. Moreover,
519 it could only be applied to systems with two end-member stations, limiting the available
520 application areas. More complex mixings can be studied by other means, such as
521 multiparameter optimum (OMP) analysis when Pa data will be available. However, OMP might
522 not be able to provide all the transport parameters as advection-diffusion-scavenging model.
523 Explicit models including scavenging like this one are essential to assess the net export of
524 nutrients or carbon to the sedimentary compartment.

525 **Acknowledgements**

526 Authors would like to acknowledge M. Boye and S. Speich, co-chief scientists of the
527 Bonus/GoodHope cruise, and all the on-board crew and sampling team, notably Amandine
528 Radic and Thomas Arsouze of BGH cruise. This work also was supported by the CNRS-INSU
529 French National program LEFE (Les Enveloppes Fluides et l'Environnement) through support
530 to the Bonus-GoodHope and AbAc projects and by the French National Research Agency
531 (ANR Bonus-Goodhope project). Authors also acknowledge two anonymous reviewers for
532 their relevant comments and advice that substantially improve the quality of the paper. Lastly,
533 this paper is dedicated to the memory of M. Roy-Barman who supervised most of this work.

534 **6. References**

535
536 Abadie, C., Lacan, F., Radic, A., Pradoux, C., Poitrasson, F., 2017. Iron isotopes reveal distinct
537 dissolved iron sources and pathways in the intermediate versus deep Southern Ocean. Proc. Natl.
538 Acad. Sci. 114, 858–863. https://doi.org/10.1073/pnas.1603107114
539 Amakawa, H., Yu, T.-L., Tazoe, H., Obata, H., Gamo, T., Sano, Y., Shen, C.-C., Suzuki, K., 2019.
540 Neodymium concentration and isotopic composition distributions in the southwestern Indian
541 Ocean and the Indian sector of the Southern Ocean. Chem. Geol. 511, 190–203.
542 https://doi.org/10.1016/j.chemgeo.2019.01.007
543 Anderson, R.F., Bacon, M.P., Brewer, P.G., 1983, Removal of ^{230}Th and ^{231}Pa from the open ocean,
544 Earth Planet. Sci. Lett., 62, 7-23, https://doi.org/10.1016/0012-821X(83)90067-5
545 Anderson, R.F., Fleisher, M.Q., Robinson, L.F., Edwards, R.L., Hoff, J.A., Moran, S.B., Loeff, M.R.
546 van der, Thomas, A.L., Roy-Barman, M., Francois, R., 2012. GEOTRACES intercalibration of
547 ^{230}Th, ^{232}Th, ^{231}Pa, and prospects for ^{10}Be. Limnol. Oceanogr. Methods 10, 179–213.
548 https://doi.org/10.4319/lom.2012.10.179
549 Bown, J., Boye, M., Baker, A., Duvieilbourg, E., Lacan, F., Le Moigne, F., Planchon, F., Speich, S.,
550 Nelson, D.M., 2011. The biogeochemical cycle of dissolved cobalt in the Atlantic and the
551 Southern Ocean south off the coast of South Africa. Mar. Chem. 126, 193–206.
552 https://doi.org/10.1016/j.marchem.2011.03.008
553 Boye, M., Wake, B.D., Lopez Garcia, P., Bown, J., Baker, A.R., Achterberg, E.P., 2012. Distributions
554 of dissolved trace metals (Cd, Cu, Mn, Pb, Ag) in the southeastern Atlantic and the Southern
555 Ocean (preprint). Biogeochemistry: Open Ocean. https://doi.org/10.5194/bgd-9-3579-2012

Branellec, P., Arhan M., Speich S., 2010. Projet GoodHope. Campagne BONUS / GOODHOPE. Rapport de données CTD-O2 . OPS/LPO/10-02

Broecker, W.S., Blanton, S., Smethie Jr., W.M., Ostlund, G., 1991. Radiocarbon decay and oxygen utilization in the Deep Atlantic Ocean. Glob. Biogeochem. Cycles 5, 87–117. https://doi.org/10.1029/90GB02279

Cavagna, A.-J., Dehairs, F., Bouillon, S., Woule-Ebongué, V., Planchon, F., Delille, B., Bouloubassi, I., 2013. Water column distribution and carbon isotopic signal of cholesterol, brassicasterol and particulate organic carbon in the Atlantic sector of the Southern Ocean. Biogeosciences 10, 2787–2801. https://doi.org/10.5194/bg-10-2787-2013

Chase, Z., Anderson, R.F., Fleisher, M.Q., Kubik, P.W., 2002. The influence of particle composition and particle flux on scavenging of Th, Pa and Be in the ocean. Earth Planet. Sci. Lett. 15.

Chever, F., Bucciarelli, E., Sarthou, G., Speich, S., Arhan, M., Penven, P., Tagliabue, A., 2010. Physical speciation of iron in the Atlantic sector of the Southern Ocean along a transect from the subtropical domain to the Weddell Sea Gyre. J. Geophys. Res. Oceans 115. https://doi.org/10.1029/2009JC005880

Condon, D.J., McLean, N., Noble, S.R., Bowring, S.A., 2010. Isotopic composition ($^{238}U/^{235}U$) of some commonly used uranium reference materials. Geochim. Cosmochim. Acta 74, 7127–7143. https://doi.org/10.1016/j.gca.2010.09.019

Deacon, G.E.R., 1979. The Weddell gyre. Deep Sea Res. Part Oceanogr. Res. Pap. 26, 981–995. https://doi.org/10.1016/0198-0149(79)90044-X

DeMaster, D.J., 1981. The supply and accumulation of silica in the marine environment. Geochim. Cosmochim. Acta 45, 1715–1732. https://doi.org/10.1016/0016-7037(81)90006-5

Deng, F., A. L. Thomas, M. J. A. Rijkenberg, and G. M. Henderson (2014), Controls on seawater ^{231}Pa, ^{230}Th and ^{232}Th concentrations along the flow paths of deep waters in the Southwest Atlantic, Earth Planet. Sci. Lett., 390(0), 93-102: http://dx.doi.org/10.1016/j.epsl.2013.12.038.

Deng, F., G. M. Henderson, M. Castrillejo, F. F. Perez, and R. Steinfeldt (2018), Evolution of ^{231}Pa and ^{230}Th in overflow waters of the North Atlantic, Biogeosciences, 15(23), 7299-7313, doi:10.5194/bg-15-7299-2018.

Edmonds, H.N., Moran, S.B., Hoff, J.A., Smith, J.N., Edwards, R.L., 1998, Protactinium-231 and Thorium-230 abundances and high scavenging rates in the western Arctic Ocean, Science, 280, 405-407, DOI: 10.1126/science.280.5362.405

Fahrbach, E., 2010. ANT-XXIV/3 report, O2 CTD report, p78-84, hdl:10013/epic.34050

Feely, R.A., Sabine, C.L., Schlitzer, R., Bullister, J.L., Mecking, S., Greeley, D., 2004. Oxygen Utilization and Organic Carbon Remineralization in the Upper Water Column of the Pacific Ocean. J. Oceanogr. 60, 45–52. https://doi.org/10.1023/B:JOCE.0000038317.01279.aa

Fripiat, F., Cavagna, A.-J., Dehairs, F., Speich, S., André, L., Cardinal, D., 2011. Silicon pool dynamics and biogenic silica export in the Southern Ocean inferred from Si-isotopes. Ocean Sci. 7, 533–547. https://doi.org/10.5194/os-7-533-2011

Garcia-Solsona, E., Jeandel, C., Labatut, M., Lacan, F., Vance, D., Chavagnac, V., Pradoux, C., 2014. Rare earth elements and Nd isotopes tracing water mass mixing and particle-seawater interactions in the SE Atlantic. Geochim. Cosmochim. Acta 125, 351–372. https://doi.org/10.1016/j.gca.2013.10.009

Gdaniec, S., Roy-Barman, M., Foliot, L., Thil, F., Dapoigny, A., Burckel, P., Garcia-Orellana, J., Masqué, P., Mörth, C.-M., Andersson, P.S., 2018. Thorium and protactinium isotopes as tracers of marine particle fluxes and deep water circulation in the Mediterranean Sea. Mar. Chem. 199, 12–23. https://doi.org/10.1016/j.marchem.2017.12.002

Gdaniec, S., Roy-Barman, M., Levier, M., Valk, O., van der Loeff, M.R., Foliot, L., Dapoigny, A., Missiaen, L., Mörth, C.-M., Andersson, P.S., 2020. ^{231}Pa and ^{230}Th in the Arctic Ocean: Implications for boundary scavenging and $^{231}Pa/^{230}Th$ fractionation in the Eurasian Basin. Chem. Geol. 532, 119380. https://doi.org/10.1016/j.chemgeo.2019.119380

Geibert, W., Usbeck, R., 2004. Adsorption of thorium and protactinium onto different particle types: experimental findings 11Associate editor: S. Krishnaswami. Geochim. Cosmochim. Acta 68, 1489–1501. https://doi.org/10.1016/j.gca.2003.10.011

Ghaleb, B., Pons-Branchu, E., Deschamps, P., 2004. Improved method for radium extraction from environmental samples and its analysis by thermal ionization mass spectrometry. J. Anal. At.

Spectrom. 19, 906. https://doi.org/10.1039/b402237h
Gouretski, V.V., Danilov, A.I., 1993. Weddell Gyre: structure of the eastern boundary. Deep Sea Res. Part Oceanogr. Res. Pap. 40, 561–582. https://doi.org/10.1016/0967-0637(93)90146-T
Guihou, A., Pichat, S., Nave, S., Govin, A., Labeyrie, L., Michel, E., Waelbroeck, C., 2010. Late slowdown of the Atlantic Meridional Overturning Circulation during the Last Glacial Inception: New constraints from sedimentary (^{231}Pa/^{230}Th). Earth Planet. Sci. Lett. 289, 520–529. https://doi.org/10.1016/j.epsl.2009.11.045
Hayes, C.T., Anderson, R.F., Fleisher, M.Q., Vivancos, S.M., Lam, P.J., Ohnemus, D.C., Huang, K.-F., Robinson, L.F., Lu, Y., Cheng, H., Edwards, R.L., Moran, S.B., 2015. Intensity of Th and Pa scavenging partitioned by particle chemistry in the North Atlantic Ocean. Mar. Chem. 170, 49–60. https://doi.org/10.1016/j.marchem.2015.01.006
Hayes, C. T., R. F. Anderson, M. Q. Fleisher, S. Serno, G. Winckler, and R. Gersonde (2014), Biogeography in ^{231}Pa/^{230}Th ratios and a balanced ^{231}Pa budget for the Pacific Ocean, Earth Planet. Sci. Lett., 391, 307-318, doi:http://dx.doi.org/10.1016/j.epsl.2014.02.001.
Jeandel, C., Venchiarutti, C., Bourquin, M., Pradoux, C., Lacan, F., Beek, P. van, Riotte, J., 2011. Single Column Sequential Extraction of Ra, Nd, Th, Pa and U from a Natural Sample. Geostand. Geoanalytical Res. 35, 449–459. https://doi.org/10.1111/j.1751-908X.2010.00087.x
Le Roy, E., Sanial, V., Charette, M.A., van Beek, P., Lacan, F., Jacquet, S.H.M., Henderson, P.B., Souhaut, M., García-Ibáñez, M.I., Jeandel, C., Pérez, F.F., Sarthou, G., 2018. The ^{226}Ra–Ba relationship in the North Atlantic during GEOTRACES-GA01. Biogeosciences 15, 3027–3048. https://doi.org/10.5194/bg-15-3027-2018
Levier, M., Roy-Barman, M., Colin, C., Dapoigny, A., 2021. Determination of low level of actinium 227 in seawater and freshwater by isotope dilution and mass spectrometry. Mar. Chem. 233, 103986. https://doi.org/10.1016/j.marchem.2021.103986
Li, Y.-H., 2005. Controversy over the relationship between major components of sediment-trap materials and the bulk distribution coefficients of ^{230}Th, ^{231}Pa, and ^{10}Be. Earth Planet. Sci. Lett. 233, 1–7. https://doi.org/10.1016/j.epsl.2005.02.023
Lin, P., Guo, L., Chen, M., 2014. Adsorption and fractionation of thorium and protactinium on nanoparticles in seawater. Mar. Chem. 162, 50–59. https://doi.org/10.1016/j.marchem.2014.03.004
Lippold, J., Luo, Y., Francois, R. et al. Strength and geometry of the glacial Atlantic Meridional Overturning Circulation. Nature Geosci 5, 813–816 (2012). https://doi.org/10.1038/ngeo1608
Livermore, B.D., Connelly, J.N., Moynier, F., Bizzarro, M., 2018. Evaluating the robustness of a consensus 238U/235U value for U-Pb geochronology. Geochim. Cosmochim. Acta 237, 171–183. https://doi.org/10.1016/j.gca.2018.06.014
Luo, S., Ku, T.-L., 2004. On the importance of opal, carbonate, and lithogenic clays in scavenging and fractionating ^{230}Th, ^{231}Pa and ^{10}Be in the ocean. Earth Planet. Sci. Lett. 220, 201–211. https://doi.org/10.1016/S0012-821X(04)00027-5
Marshall, J., Speer, K., 2012. Closure of the meridional overturning circulation through Southern Ocean upwelling. Nat. Geosci. 5, 171–180. https://doi.org/10.1038/ngeo1391
McManus, J. F., R. Francois, J.-M. Gherardi, L. D. Keigwin, and S. Brown-Leger (2004), Collapse and rapid resumption of Atlantic meridional circulation linked to deglacial climate changes, Nature, 428, 834– 837, https://doi.org/10.1038/nature02494
Nicholls, K.W., Østerhus, S., Makinson, K., Gammelsrød, T., Fahrbach, E., 2009. Ice-ocean processes over the continental shelf of the southern Weddell Sea, Antarctica: A review. Rev. Geophys. 47, RG3003. https://doi.org/10.1029/2007RG000250
Pavia, F.J., Anderson, R.F., Pinedo-Gonzalez, P., Fleisher, M.Q., Brzezinski, M.A., Robinson, R.S., 2020. Isopycnal Transport and Scavenging of ^{230}Th and ^{231}Pa in the Pacific Southern Ocean. Glob. Biogeochem. Cycles 34. https://doi.org/10.1029/2020GB006760
Robinson, S., Ivanovic, R., van de Flierdt, T., Blanchet, C.L., Tachikawa, K., Martin, E.E., Cook, C.P., Williams, T., Gregoire, L., Plancherel, Y., Jeandel, C., Arsouze, T., 2021. Global continental and marine detrital εNd: An updated compilation for use in understanding marine Nd cycling. Chem. Geol. 567, 120119. https://doi.org/10.1016/j.chemgeo.2021.120119
Roy-Barman, M., Thil, F., Bordier, L., Dapoigny, A., Foliot, L., Ayrault, S., Lacan, F., Jeandel, C., Pradoux, C., Garcia-Solsona, E., 2019. Thorium isotopes in the Southeast Atlantic Ocean:

Tracking scavenging during water mass mixing along neutral density surfaces. Deep Sea Res. Part Oceanogr. Res. Pap. 149, 103042. https://doi.org/10.1016/j.dsr.2019.05.002

Rutgers van der Loeff, M., Moore, W.S., 1999. Determination of natural radioactive tracers., in: Methods of Seawater Analysis. pp. 365–397.

Rutgers van der Loeff, M., Venchiarutti, C., Stimac, I., van Ooijen, J., Huhn, O., Rohardt, G., Strass, V., 2016. Meridional circulation across the Antarctic Circumpolar Current serves as a double ^{231}Pa and ^{230}Th trap. Earth Planet. Sci. Lett. 455, 73–84. https://doi.org/10.1016/j.epsl.2016.07.027

Rutgers van der Loeff, M.M., Berger, G.W., 1993. Scavenging of ^{230}Th and ^{231}Pa near the antarctic polar front in the South Atlantic. Deep Sea Res. Part Oceanogr. Res. Pap. 40, 339–357. https://doi.org/10.1016/0967-0637(93)90007-P

Ryan, S., Schröder, M., Huhn, O., Timmermann, R., 2016. On the warm inflow at the eastern boundary of the Weddell Gyre. Deep Sea Res. Part Oceanogr. Res. Pap. 107, 70–81. https://doi.org/10.1016/j.dsr.2015.11.002

Sarmiento, J.L., Gruber, N., Brzezinski, M.A., Dunne, J.P., 2004. High-latitude controls of thermocline nutrients and low latitude biological productivity. Nature 427, 56–60. https://doi.org/10.1038/nature02127

Schlitzer, R et al., 2018, The GEOTRACES Intermediate Data Product 2017, Chemical Geology, 493, 210-223, https://doi.org/10.1016/j.chemgeo.2018.05.040

Scholten, J.C., Fietzke, J., Mangini, A., Garbe-Schönberg, C.-D., Eisenhauer, A., Schneider, R., Stoffers, P., 2008. Advection and scavenging: Effects on ^{230}Th and ^{231}Pa distribution off Southwest Africa. Earth Planet. Sci. Lett. 271, 159–169. https://doi.org/10.1016/j.epsl.2008.03.060

Schröder, M., Fahrbach, E., 1999. On the structure and the transport of the eastern Weddell Gyre. Deep Sea Res. Part II Top. Stud. Oceanogr. 46, 501–527. https://doi.org/10.1016/S0967-0645(98)00112-X

Sokolov, S., Rintoul, S.R., 2009. Circumpolar structure and distribution of the Antarctic Circumpolar Current fronts: 1. Mean circumpolar paths. J. Geophys. Res. Oceans 114. https://doi.org/10.1029/2008JC005108

Stichel, T., Frank, M., Rickli, J., Hathorne, E.C., Haley, B.A., Jeandel, C., Pradoux, C., 2012a. Sources and input mechanisms of hafnium and neodymium in surface waters of the Atlantic sector of the Southern Ocean. Geochim. Cosmochim. Acta 94, 22–37. https://doi.org/10.1016/j.gca.2012.07.005

Venchiarutti, C., van der Loeff, M.R., Stimac, I., 2011. Scavenging of ^{231}Pa and thorium isotopes based on dissolved and size-fractionated particulate distributions at Drake Passage (ANTXXIV-3). Deep Sea Res. Part II Top. Stud. Oceanogr., Physics, Carbon Dioxide, Trace Elements and Isotopes in the Southern Ocean: The Polarstern Expeditions ANT XXIV-3 (2008) and ANT XXIII/3 (2006) 58, 2767–2784. https://doi.org/10.1016/j.dsr2.2010.10.040

Walter, H.J., Rutgers van der Loeff, M.M., Hoeltzen, H., 1997. Enhanced scavenging of ^{231}Pa relative to +Th in the South Atlantic south of the Polar Front: Implications for the use of the ^{231}Pa/^{230}Th ratio as a paleoproductivity proxy. Earth Planet. Sci. Lett. 149, 85–100. https://doi.org/10.1016/S0012-821X(97)00068-X

Winogradow, A., Mackiewicz, A., Pempkowiak, J., 2019. Seasonal changes in particulate organic matter (POM) concentrations and properties measured from deep areas of the Baltic Sea. Oceanologia 61, 505–521. https://doi.org/10.1016/j.oceano.2019.05.004

Yu, E.-F., Francois, R., Bacon, M.P., 1996. Similar rates of modern and last-glacial ocean thermohaline circulation inferred from radiochemical data. Nature 379, 689–694. https://doi.org/10.1038/379689a0

Electronic Support :

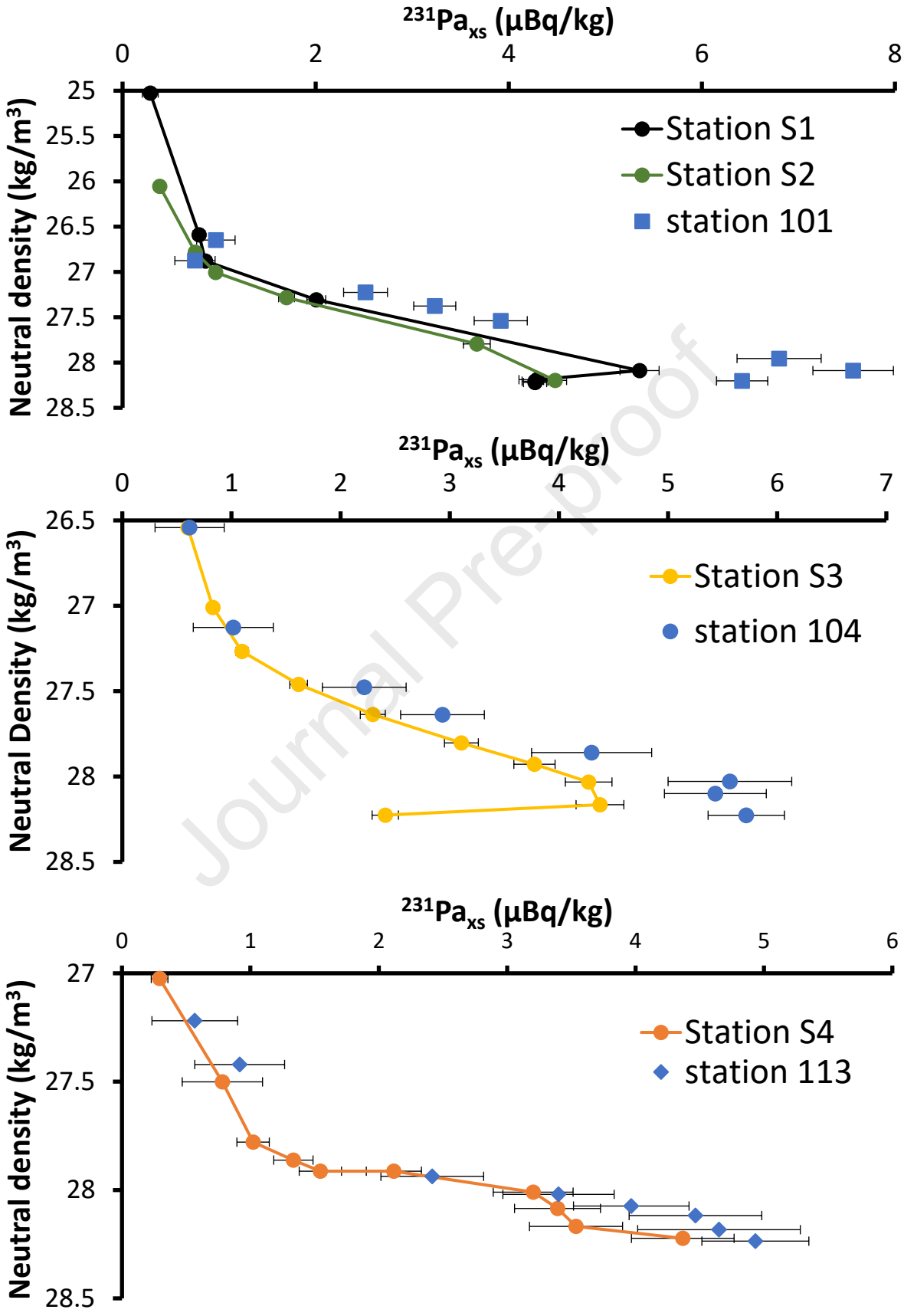

Figure ES1 : $^{231}Pa_{xs\text{-}dissolved}$ versus neutral during the Bonus GoodHope and ZeroDrake cruises at hydrologically close stations.

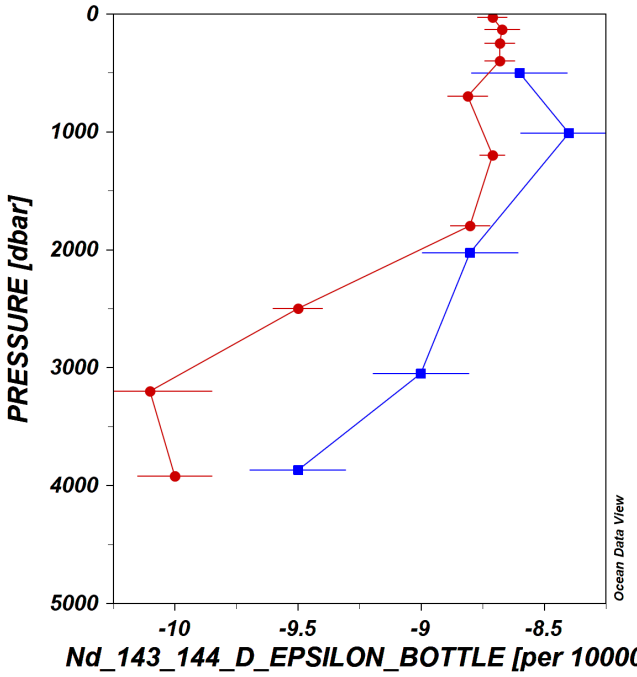

719

Figure ES2 : Comparison of epsilon Nd signature of BGH station S5 (red dot)(Garcia-Solsona et al. 2014) and the ZeroDrake station 131 (blue dot) (Stichel et al. 2012) compiled in the GEOTRACES intermediate report IDP2017 (Schlitzer et al., 2018)

720

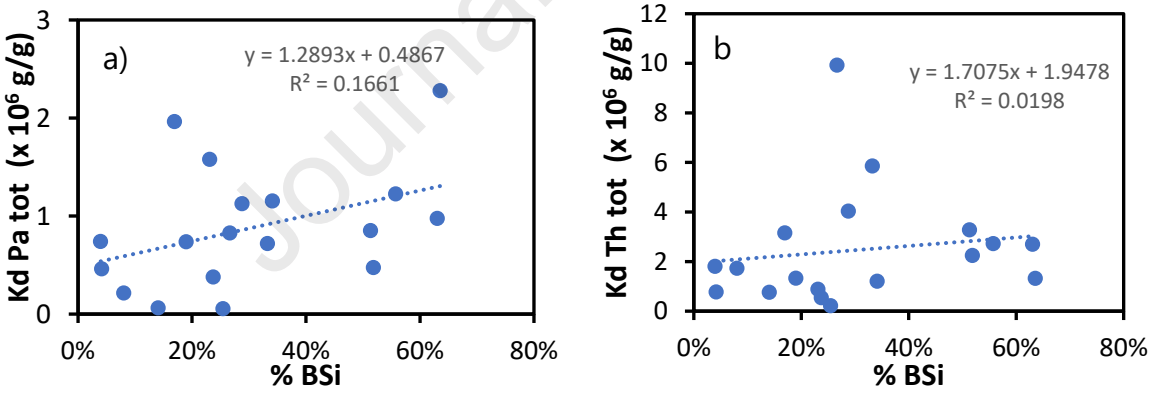

721

Figure ES3 : K_d estimated from the particulate and dissolved fraction, (a) for the ^{231}Pa and (b) for the ^{230}Th, against the estimated proportion of biogenic silica in the particulate fraction

722

723

724

725

726

Table ES1 : Dissolved concentration of ^{231}Pa from samples of the Bonus GoodHope cruise

Station	Depth (m)	θ (°C)	Salinity	γ^n (kg/m^3)	$^{231}Pa_d$ (µBq/kg)	$^{231}Pa_{d\text{-}xs}$ (µBq/kg)	O_2 (µmol/kg)	Water mass
Station S1: 36.50°S, 13.10°E, 4923 m bottom depth								
	29	20.785	35.617	25.0222	0.33 ± 0.05	0.33 ± 0.05	233	ICW
	198	12.364	35.014	26.53	0.88 ± 0.03	0.88 ± 0.03	223	ICW
	397	9.824	34.757	26.7918	1.02 ± 0.04	1.02 ± 0.04	230	ICW
	753	4.973	34.346	27.1602	2.20 ± 0.05	2.19 ± 0.05	198	i-AAIW
	3005	1.945	34.836	27.8444	5.88 ± 0.11	5.88 ± 0.11	227	SE-NADW
	3981	0.892	34.749	27.8506	4.91 ± 0.11	4.90 ± 0.11	218	AABW
	4565	0.716	34.733	27.8493	5.03 ± 0.08	5.02 ± 0.08	217	AABW
	4907	0.568	34.72	27.8481	5.57 ± 0.08	5.55 ± 0.08	219	AABW
Station S2: 42.47°S, 08.93°E, 4070 m bottom depth								
	20	12.951	34.521	26.0547	0.41 ± 0.02	0.41 ± 0.02	272	ICW
	124	9.083	34.482	26.7815	0.82 ± 0.03	0.82 ± 0.03	262	ICW
	292	6.654	34.267	27.0053	1.07 ± 0.03	1.07 ± 0.03	273	ICW/a-AAIW
	595	4.138	34.185	27.2829	1.88 ± 0.04	1.88 ± 0.04	254	a-AAIW
	1453	2.626	34.585	27.7945	3.99 ± 0.08	3.98 ± 0.08	181	UCDW
	4021	0.81	34.741	28.1961	5.11 ± 0.07	5.11 ± 0.07	219	AABW
Station S3: 47.55°S, 04.37°E, 4480 m bottom depth								
	40	6.32	33.733	26.5685	0.63 ± 0.05	0.63 ± 0.05	303	AASW
	124	4.029	33.867	27.0072	0.90 ± 0.05	0.89 ± 0.05	306	AASW
	248	3.633	34.101	27.2697	1.22 ± 0.05	1.22 ± 0.05	272	AASW/a-AAIW
	495	2.739	34.233	27.4888	1.80 ± 0.05	1.79 ± 0.05	229	a-AAIW
	742	2.591	34.407	27.6574	2.52 ± 0.05	2.52 ± 0.05	189	a-AAIW/UCDW
	1068	2.447	34.575	27.8099	3.40 ± 0.07	3.40 ± 0.07	175	A_UCDW
	1482	2.334	34.716	27.936	4.16 ± 0.11	4.16 ± 0.11	186	SW-NADW
	2003	1.971	34.771	28.0376	4.72 ± 0.12	4.72 ± 0.12	203	SW-NADW
	3052	0.955	34.731	28.1653	4.85 ± 0.09	4.85 ± 0.09	210	SW-NADW
	4299	0.415	34.695	28.2262	2.92 ± 0.07	2.92 ± 0.07	213	AABW
Station S4: 51.85°S, 00.00°E, 2570 m bottom depth								
	59	2.521	33.712	27.0277	0.33 ± 0.04	0.33 ± 0.04	330	AASW
	168	0.827	34.033	27.4838	0.88 ± 0.18	0.88 ± 0.18	281	WW (AASW)
	248	1.543	34.433	27.7832	1.20 ± 0.07	1.20 ± 0.07	199	WW/DP-UCDW
	327	1.811	34.548	27.8553	1.57 ± 0.09	1.57 ± 0.09	178	DP-UCDW
	416	1.874	34.627	27.9165	1.85 ± 0.10	1.85 ± 0.10	175	DP-UCDW
	416	1.874	34.627	27.9165	2.40 ± 0.12	2.39 ± 0.12	175	DP-UCDW
	742	1.702	34.704	28.012	3.63 ± 0.18	3.63 ± 0.18	186	LCDW
	1117	1.42	34.727	28.08	3.93 ± 0.19	3.93 ± 0.19	199	LCDW
	1678	0.755	34.704	28.171	4.12 ± 0.21	4.12 ± 0.21	207	LCDW/AABW
	2307	0.359	34.689	28.225	5.00 ± 0.23	5.00 ± 0.23	212	AABW
Intercal: 52.98°S, 00.00°E, 2624 m bottom depth								
	380	1.81	34.63	27.929	2.70 ± 0.07	2.70 ± 0.07	179	UCDW
	500	1.78	34.68	27.979	3.16 ± 0.07	3.16 ± 0.07	183	LCDW
	1000	1.22	34.71	28.094	4.28 ± 0.09	4.28 ± 0.09	201	LCDW
Station S5: 57.55°S, 00.03°W, 3932 m bottom depth								
	30	0.40	34.078	27.559	1.25 ± 0.06	1.25 ± 0.06	344	WW(AASW)
	134	-0.671	34.355	27.8713	0.74 ± 0.07	0.74 ± 0.07	292	WW(AASW)
	396	0.529	34.674	28.154	3.25 ± 0.05	3.25 ± 0.05	206	WDW
	692	0.422	34.685	28.202	3.35 ± 0.16	3.35 ± 0.16	201	WDW
	1185	0.154	34.677	28.2434	4.03 ± 0.02	4.03 ± 0.02	215	WDW/WSDW
	1776	-0.104	34.668	28.2872	4.22 ± 0.10	4.22 ± 0.10	225	WDW/WSDW
	2462	-0.346	34.66	28.332	3.74 ± 0.14	3.74 ± 0.14	235	WSDW
	3848	-0.632	34.65	28.385	6.09 ± 0.11	6.09 ± 0.11	248	WSDW/WSBW

727

728

Table ES2 : Particulate ^{231}Pa from Bonus GoodHope samples and the FTh/Pa measured from the particulate measurement and a linear interpolation over dissolved sample. $^{230}Th_{p\text{-}xs}$ converted in µBq/kg from Roy-Barman et al. 2019 and BSi from Fripiat et al. 2011

Depth (m)	$^{231}Pa_p$ (µBq/kg)		$^{230}Th_{p\text{-}xs}$ (µBq/kg)		$^{231}Pa_{p\text{-}xs}$ (µBq/kg)		BSi (µg/kg)	Pa_p/Pa_d (%)	FTh/Pa	
Station S1										
30	0.011	±0.002	0.035	±0.002	0.009	±0.002	18.82	1.50	2.41	±0.55
199	0.009	±0.002	0.098	±0.003	0.007	±0.002		0.5	10.53	±1.76
1242	0.030	±0.005	1.004	±0.023	0.028	±0.005		0.42*	26.55	±4.19
2687	0.035	±0.005	0.877	±0.002	0.032	±0.005		0.24*	15.52	±2.48
2732	0.026	±0.004	1.304	±0.31	0.026	±0.004		0.18*	27.41	±7.89
4628	0.601	±0.095	20.32	±0.31	0.573	±0.092		5.56	10.60	±1.74
Station S2										
20	0.030	±0.007	0.100	±0.003	0.028	±0.007	2.7	3.31	2.95	±0.7
257	0.012	±0.005	0.261	±0.002	0.012	±0.005		0.57	13.10	±5.99
601	0.012	±0.004	0.360	±0.003	0.012	±0.004		0.33	14.61	±4.11
1426	0.018	±0.007	1.090	±0.007	0.018	±0.007		0.21	37.63	±16.25
1941	0.011	±0.002	0.548	±0.004	0.011	±0.002		0.11*	25.82	±4.16
2859	0.025	±0.004	1.219	±0.008	0.023	±0.004		0.23*	23.07	±5.24
3858	0.187	±0.030	6.211	±0.054	0.181	±0.028		1.73	13.19	±2.14
Station S3										
40	0.005	±0.002	0.102	±0.002	0.005	±0.002	21.50	0.94	16.49	±5.87
594	0.032	±0.004	0.511	±0.002	0.030	±0.004	6.72	1.33*	8.452	±1.24
1058	0.035	±0.005	0.784	±0.002	0.035	±0.005	3.36	1.03	12.41	±1.72
1985	0.041	±0.005	1.075	±0.003	0.041	±0.005		0.85	12.58	±1.80
3025	0.048	±0.007	1.338	±0.005	0.046	±0.007		0.96	12.53	±2.11
4262	0.037	±0.005	0.255	±0.002	0.037	±0.005		1.25	3.12	±0.47
Station S4										
59	0.002	±0.000	0.015	±0.0004	0.002	±0.000	20.16	0.42	3.83	±0.90
169	0.033	±0.002	0.225	±0.001	0.033	±0.002	24.86	3.70	2.66	±0.54
258	0.049	±0.007	0.350	±0.001	0.049	±0.007	18.82	3.97	2.23	±0.35
743	0.053	±0.002	0.515	±0.002	0.053	±0.002	8.74	5.30	3.88	±0.21
1119	0.033	±0.000	0.473	±0.002	0.033	±0.000	9.41	3.91	4.67	±0.26
1682	0.023	±0.004	0.550	±0.002	0.021	±0.004	2.02	4.02	7.89	±1.19
2273	0.144	±0.019	1.425	±0.004	0.144	±0.019	7.39	9.47	3.63	±0.52
2469	0.203	±0.028	1.398	±0.004	0.203	±0.026		9.74		
Station S5										
30	0.048	±0.007	0.534	±0.004	0.048	±0.007				
139	0.041	±0.002	0.192	±0.002	0.041	±0.002	8.064	5.22	0.57	±0.06
248	0.139	±0.005	0.380	±0.002	0.139	±0.005	15.46	5.92*	0.57	±0.03
694	0.076	±0.012	0.413	±0.008	0.076	±0.012	6.72	2.22	1.05	±0.20
1784	0.055	±0.005	0.534	±0.005	0.055	±0.005	3.36	1.29	1.81	±0.20
2478	0.111	±0.004	1.296	±0.023	0.111	±0.004	2.69	2.89	1.68	±0.10
3172	0.157	±0.005	1.306	±0.005	0.157	±0.005	2.69	3.44*	1.58	±0.08
3840	0.315	±0.011	2.187	±0.009	0.314	±0.011		3.06	1.62	±0.08

*Pa_d used are interpolated one to the particulate sampling depth following a curve derived from the Weddell gyre scavenging model (Rutgers van Der Loeff, 1993)

Table ES3 : Major phases in filtered particles and Th and Pa partition coefficients for the bulk particulate matter and Pa partition coefficient estimated for pure opal.

station	depth (m)	Bsi (µg/kg)	$CaCO_3$ (µg/kg)	^{232}Th (pg/kg)	POM (µg/kg)	SPM (µg/kg)	% Opal (g/g)	$K_{d\text{-}bulk}$(Pa) $\times 10^6$ (g/g)	$K_{d\text{-}bulk}$(Th) $\times 10^6$ (g/g)	$K_{d\text{-}opal}$(Pa)* $\times 10^6$ (g/g)
1	25	18.82	33	6.96	26.7	79.2	24 %	0.378	0,536	-
2	70	2.69	19	6.49	45.6	67.9	4 %	0.741	1,803	1.62
3	41	21.50	55.2	7.06	75.4	152.8	14 %	0.062	0,757	-
3	600	6.72	5.7	4.41	7.4	20.2	33 %	0.719	5,848	0.59
3	1068	3.36	4.3	5.07	4.4	12.6	27 %	0.826	9,920	0.81
4	60	20.16	19	0.07	40	79.2	25 %	0.054	0,212	-
4	170	24.86	2.4	1.39	12.0	39.4	63 %	0.975	2,692	1.16
4	260	18.82	6.3	2.37	8.4	33.8	56 %	1.225	2,721	1.60
4	749	8.74	2.5	2.21	5.6	17.0	51 %	0.851	3,274	0.96
4	1128	9.41	2.5	2.76	6.0	18.1	52 %	0.474	2,243	0.23
4	1695	2.02	17	2.14	5.8	25.0	8 %	0.214	1,726	-
4	2305	7.39	12	6.06	5.7	25.7	29 %	1.125	4,029	1.80
5	140	8.06	6.4	2.09	20.2	34.9	23 %	1.578	0,881	4.55
5	250	15.46	2.1	2.42	6.5	24.3	64 %	2.279	1,315	3.17
5	700	6.72	3.1	3.48	9.5	19.7	34 %	1.153	1,199	2.00
5	1800	3.36	12.1	3.93	1.8	17.7	19 %	0.737	1,324	0.04
5	2500	2.69	58	8.31	3.0	64.5	4 %	0.460	0,768	-
5	3200	2.69	7	11.03	5.1	15.9	17 %	1.962	3,151	7.15

BSi from Fripiat and al. 2011, POM estimated from the POC (Cavagna et al., 2013) and ^{232}Th from Roy-Barman and al. 2019

* The $K_{d\text{-}opal}(^{231}Pa)$ reported here are only ones with the opal contribution to the total partition is significant toward the other phases of the particulate matter

Highlights:

- Measurements of ^{231}Pa in new seawater samples from the Atlantic sector of Southern Ocean
- New determination of the partition coefficient of the ^{231}Pa on the opal particle phase
- Assessment of the advection-diffusion-scavenging model along isopycnal by an application to the ^{231}Pa data across the Southern Ocean

Declaration of interests

☒ The authors declare that they have no known competing financial interests or personal relationships that could have appeared to influence the work reported in this paper.

☐ The authors declare the following financial interests/personal relationships which may be considered as potential competing interests: